Cloud response to co-condensation of water and organic vapors over the boreal forest

Liine Heikkinen[1,2], Daniel G. Partridge[3], Sara Blichner[1,2], Wei Huang[4], Rahul Ranjan[1,2], Paul Bowen[3], Emanuele Tovazzi[3], Tuukka Petäjä[4], Claudia Mohr[1,2], and Ilona Riipinen[1,2]

[1]Department of Environmental Science (ACES), Stockholm University, Stockholm, Sweden
[2]Bolin Centre for Climate Research, Stockholm University, Stockholm, Sweden
[3]Department of Mathematics and Statistics, Faculty of Environment, Science and Economy, University of Exeter, Exeter, United Kingdom
[4]Institute for Atmospheric and Earth System Research (INAR) / Physics, University of Helsinki, Helsinki, Finland

Correspondence to: Liine Heikkinen (liine.heikkinen@aces.su.se) and Ilona Riipinen (ilona.riipinen@aces.su.se)

Abstract

Accounting for the condensation of organic vapors along with water vapor (co-condensation) has been shown in adiabatic cloud parcel model (CPM) simulations to enhance the number of aerosol particles that activate to form cloud droplets. The boreal forest is an important source of biogenic organic vapors, but the role of these vapors in co-condensation has not been systematically investigated. In this work, the environmental conditions under which strong co-condensation -driven cloud droplet number enhancements would be expected over the boreal biome are identified. Recent measurement technology, specifically the Filter Inlet for Gases and AEROsols (FIGAERO) coupled to an iodide-adduct Chemical Ionization Mass Spectrometer (I-CIMS), is utilized to construct a volatility distribution of the boreal atmospheric organics. Then, a suite of CPM simulations initialized with a comprehensive set of concurrent aerosol observations collected in the boreal forest of Finland during Spring 2014 is performed. The degree to which co-condensation impacts droplet formation in the model is shown to be dependent on the initialization of temperature, relative humidity, updraft velocity, aerosol size distribution, organic vapor concentration and the volatility distribution. The predicted median enhancements in cloud droplet number concentration (CDNC) due to accounting for the co-condensation of water and organics fall on average between 16 and 22%. This corresponds to activating particles 10–16 nm smaller in dry diameter, that would otherwise remain as interstitial aerosol. The highest CDNC enhancements (ΔCDNC) are predicted in the presence of a nascent ultrafine aerosol mode with a geometric mean diameter of ~40 nm and no clear Hoppel minimum, indicative of pristine environments with a source of ultrafine particles (e.g., via new particle formation processes). Such aerosol size distributions are observed 30–40% of the time in the studied boreal forest environment in spring and fall when new particle formation frequency is the highest. Five years of UK Earth System Model (UKESM1) simulations are further used to evaluate the frequencies to which such distributions are experienced by an Earth System Model over the whole boreal biome. The frequencies are substantially lower than those observed at the boreal forest measurement site (<6% of the time) and the positive values, peaking in spring, are modeled only over Fennoscandia and western parts of Siberia. Overall, the similarities in the size distributions between observed and modeled (UKESM1) are limited, which would limit the ability of this model, or any model with a similar aerosol representation, to project the climate-relevance of co-condensation. For the critical aerosol size distribution regime, ΔCDNC is shown to be sensitive to the concentrations of semi-volatile and some intermediate-volatility organic compounds (SVOCs and IVOCs) especially when the overall particle surface area is low. The magnitudes of ΔCDNC remain less affected by the more volatile vapors such as formic acid and extremely low and low volatility organic compounds (ELVOCs and LVOCs). The reasons for this are that most

43 volatile organic vapors condense inefficiently due to their high volatility below cloud base and the concentrations

44 of LVOCs and ELVOCs are too low to gain significant concentrations of soluble mass to reduce critical

45 supersaturations enough for droplet activation to occur. Reduction of the critical supersaturation caused by organic

46 condensation emerges as the main driver of the modeled ΔCDNC. The results highlight the potential significance

47 of co-condensation in pristine boreal environments close to sources of fresh ultrafine particles. For accurate

48 predictions of co-condensation effects on CDNC, also in larger scale models, an accurate representation of the

49 aerosol size distribution is critical. Further studies targeted at finding observational evidence and constraints for

50 co-condensation in the field are encouraged.

51

1 Introduction

53 Boreal forests emit significant quantities of volatile organic compounds (VOCs, Guenther et al., 1995; Artaxo et

54 al., 2022), such as monoterpenes, that undergo oxidation in the atmosphere. The condensable oxidation products

55 contribute considerably to the secondary organic aerosol (SOA) mass concentrations in the boreal forest air (e.g.,

56 Tunved et al., 2006; Artaxo et al., 2022). The emissions of monoterpenes are strongly temperature-dependent,

57 which leads – together with the higher oxidative potential in the sunlit months – to highest biogenic SOA

58 concentrations in summer (Paasonen et al., 2013; Heikkinen et al., 2020; Mikhailov et al., 2017). This has recently

59 been shown to have implications for cloud properties above the boreal forest through the availability of more

60 cloud condensation nuclei (CCN; Yli-Juuti et al., 2021; Petäjä et al., 2022; Paasonen et al., 2013). Under constant

61 meteorological conditions in the boreal forest, an increase in aerosol concentration typically results in an increase

62 in cloud droplet number concentration (CDNC) and smaller average droplet size for a given liquid water content

63 (Yli-Juuti et al., 2021). These effects alter the cloud brightness making clouds scatter incoming solar radiation

64 more efficiently (Twomey effect; Twomey, 1974, 1977). The relationships between the number of aerosol

65 particles, CDNC, and their effects on climate are, however, non-linear and complex, which makes aerosol-cloud

66 interactions the largest source of uncertainty in radiative forcing estimates from climate models (e.g., Lohmann

67 and Feichter, 2005; Carslaw et al., 2013; Bellouin et al., 2020). The development of "bottom-up" predictive

68 models is needed for providing accurate, yet robust, simplifications of key processes involved in aerosol-cloud

69 interactions – eventually for inclusion in climate models in computationally efficient parameterizations.

70 Numerous studies have been carried out to understand the role of condensable organic vapors in SOA

71 formation (e.g., Hallquist et al., 2009; Shrivastava et al., 2017) and hence the concentrations of CCN (i.e. particles

72 of at least 50–100 nm in diameter for the water vapor supersaturations typical of the boreal environments; Cerully

73 et al., 2011; Sihto et al., 2011; Paramonov et al., 2013; Hong et al., 2014; Paramonov et al., 2015). The yields of

74 volatile, intermediate-volatility or semi-volatile organic compounds (VOCs, IVOCs, or SVOCs) from

75 monoterpene oxidation, such as those of pinonaldehyde, formic acid, or acetic acid, are generally much higher

76 than those of the readily condensable lower-volatility vapors (low-volatility organic compounds, LVOCs and

77 extremely low volatility organic compounds, ELVOCs), but they are typically not considered directly important

78 for SOA or CCN formation. The above-mentioned volatility classes are determined based on the volatilities of

79 individual compounds binned into a volatility basis set (VBS; Donahue et al., 2006): VOCs have a saturation

80 vapor concentration (C^*; given in units of μg m^{-3} throughout the paper) of at least 10^7 μg m^{-3}, IVOCs are distributed

81 in the C^* range of [10^3, 10^6] μg m^{-3}, SVOCs of [1, 100], LVOCs of [10^{-3}, 10^{-1}] and ELVOCs have a C^* below 10$^-$

82 [4] µg m^{-3} (e.g., Donahue et al., 2011). While VOCs, IVOCs, and some SVOCs are unlikely to produce significant
83 concentrations of SOA at ground level without additional oxidation steps or multiphase chemistry, some of them
84 can condense at higher altitudes if transported aloft (e.g., Murphy et al., 2015). In addition, aerosol liquid water
85 plays a key role in determining the amount of SVOCs and IVOCs in the condensed phase. Liquid water acts as an
86 absorptive medium, and a higher liquid water content can enable a higher quantity of organic vapors to partition
87 into the condensed phase. However, the role of water in determining partitioning coefficients is often neglected
88 when absorptive partitioning theory (Pankow et al., 2001) is applied. Barley et al. (2009) demonstrated that the
89 inclusion of water, when predicting absorptive partitioning using Raoult's law, could lead to evident increases in
90 organic aerosol (OA) mass concentrations under atmospherically relevant OA loadings. Later work by Topping
91 and McFiggans (2012) showed how under a decreasing temperature trend, the concentration of aerosol liquid
92 water increases making the solution particle more dilute enabling enhanced dynamic partitioning of organic vapors
93 (together with water vapor). This work focuses on the dynamic SVOC and IVOC condensation together with
94 water vapor (co-condensation) in rising and cooling air motions, and the effects co-condensation poses on cloud
95 microphysics.

96 Warm (liquid) clouds can form when air rises and cools, eventually leading to the air being supersaturated
97 with water vapor. The excess water vapor condenses onto aerosol particles, rapidly growing them into cloud
98 droplets. While water represents the most abundant vapor in the atmosphere, also other trace species can influence
99 the cloud droplet activation process as the cooling of the rising air triggers also their condensation. The partitioning
100 of these other vapors is partially driven by the decrease in temperature itself, which makes the species less volatile,
101 but more important it is the increase in aerosol liquid water, and the dilution of the aerosol solution that enables
102 them to partition to the liquid phase (Topping and McFiggans, 2012). As the trace vapors condense in the rising
103 air under sub-saturated conditions, the molar fraction of water in the swelling aerosol particles increases slower
104 than in the absence of this co-condensation process, which in turn leads to the condensation of additional water
105 by the time the air parcel reaches lifting condensation level. The co-condensation of water with other trace vapors
106 eventually leads to a reduction in critical supersaturation (s^*) required for droplet activation of the particles due to
107 an increased amount of organic solute (Topping and McFiggans, 2012), as described by Köhler theory (Köhler,
108 1936). Topping et al. (2013) studied the impact of organic co-condensation on CDNC using a cloud parcel model
109 (CPM) initialized with a suite of realistic conditions describing the aerosol particle number size distribution
110 (PNSD), composition, and OA volatility distribution. They showed significant enhancements in CDNC (ΔCDNC
111 up to roughly 50%) when comparing simulations with organic condensation (CC) to simulations without it
112 (noCC). In addition to co-condensing organics and water, also co-condensation of nitric acid and ammonia
113 together with water has been suggested to enhance CDNC in earlier process modeling studies (e.g., Kulmala et
114 al., 1993; Korhonen et al., 1996; Hegg, 2000; Romakkaniemi et al., 2005). Direct experimental studies of co-
115 condensation remain challenging, however, as aerosol particles are typically dried during the sampling process
116 and the loss of liquid water may lead to evaporation of co-condensed organics, too. While direct observational
117 evidence of co-condensation is scarce, recent laboratory studies show significant water uptake due to co-
118 condensation of propylene glycol and water onto ammonium sulfate particles (Hu et al., 2018). In addition,
119 ambient observations from Delhi and Beijing suggest co-condensation of hydrochloric acid (HCl) or nitric acid
120 (HNO$_3$) with water vapor, respectively, to be of essence in reproducing particle hygroscopicities corresponding
121 to the visibility measurements during haze events (Gunthe et al., 2021; Wang et al., 2020).

The cloud response to co-condensation in the form of ΔCDNC has been previously shown to result from the complex interplay between updraft velocity, PNSD and organic compound volatility distribution (Topping et al., 2013). For the same amount of organic vapor, Topping et al. (2013) modelled a non-linear updraft response of ΔCDNC. The highest ΔCDNC were obtained when updrafts were below 1 m s^{-1}, but the peak ΔCDNC was dependent on the initial PNSD characteristics. Under higher updrafts, the modelled ΔCDNC was found to decrease exponentially as a function of updraft, but the plateau of the curve depended on the initial PNSD – although the dependence on the exact parameters describing multimodal PNSD were not extensively explored. If assumed representative of the global continents, ΔCDNC values of tens of percent could impose a significant impact on predictions of cloud albedo and the Earth's radiative budget. In fact, Topping et al. (2013) suggest accounting for co-condensation could result in up to 2.5% increase in cloud albedo (corresponding to global ΔCDNC = 40%). This albedo increase would translate into a –1.8 W m^{-2} change in the global cloud radiative effect over land. Topping et al. (2013) stress, however, that the impacts of co-condensation will be spatially heterogeneous because of variable surface albedo and variation in VOC sources. For comparison, one should note that the net radiative effect of clouds is approximately –20 W m^{-2} (Boucher et al., 2013). The recent best estimate of the effective radiative forcing from aerosol-cloud interactions is, on the other hand, –1.0 [–1.7 to –0.3] W m^{-2} (Forster et al., 2021). The potential contribution of co-condensation to estimates of radiative forcing due to aerosol–cloud–climate feedbacks remains unclear.

Boreal forests make up about one third of the Earth's forested area, which makes the boreal biome an important source of biogenic organic vapors that could affect droplet activation in warm clouds through co-condensation. ΔCDNC due to co-condensation over the boreal forest could reduce the albedo over the dark boreal forest canopy. In a warming climate, temperature-dependent biogenic terpene emissions (Guenther et al., 1993) are expected to rise (e.g., Turnock et al., 2020). These increasing emissions enrich the ambient pool of organics available for condensation in rising air. As suggested in Topping et al. (2013), through the effects organic co-condensation poses on CDNC, organic co-condensation could enhance the proposed negative climate feedback mechanism associated with the biogenic SOA (Kulmala et al., 2004; Spracklen et al., 2008; Kulmala et al., 2014; Yli-Juuti et al., 2021), the magnitude of which is currently highly uncertain (Thornhill et al., 2021; Sporre et al., 2019; Scott et al., 2018; Paasonen et al., 2013; Sporre et al., 2020).

Since the publication of the Topping et al. (2013) study, improved constraints of the effective volatilities of organic aerosol (e.g., Thornton et al., 2020) are available through the application of chemical ionization mass spectrometers (CIMS) providing molecular level information on gas- and particle-phase composition in near-real time. With the up-to-date volatility parameterizations using the molecular formulae retrieved from CIMS data, volatility distributions can be calculated along a volatility scale ranging from ELVOCs to VOCs, while previous techniques could not enable constraints on volatilities exceeding $C^* = 1000$ μg m^{-3} (Cappa and Jimenez, 2010). This means that a notable amount of semi- and intermediate volatility vapors with high co-condensation potential were not included in the early organic co-condensation work (Topping et al., 2013; Crooks et al., 2018). The recent methodological developments motivate revisiting work of Topping et al. (2013), as potentially large concentrations of condensable organic vapors have been so far neglected.

In this study, the cloud response to the co-condensation of organic vapors over the boreal forest of Finland is investigated using a CPM. Measurements and parameterization techniques involving FIGAERO-I-CIMS data are utilized to constrain the volatility distribution of organics for these simulations. In addition, to

ensure realistic modeling scenarios, simultaneously recorded measurements of PNSD and chemical composition from the Aerosol Chemical Speciation Monitor (ACSM) are used for the CPM initialization. 97 unique CPM simulations are performed, initialized with conditions from boreal spring and early summer following measurement time series recorded during the Biogenic Aerosols – Effects on Clouds and Climate (BAECC) campaign at the Station Measuring Atmosphere–Ecosystem Relationships (SMEAR) II (Hari and Kulmala, 2005) in Finland (Petäjä et al., 2016) and the sensitivity to meteorological conditions is studied. These simulations are then used to characterize the environmental conditions (with respect to the size distribution and organic aerosol volatility distribution characteristics) that promote co-condensation-driven CDNC enhancements in the boreal atmosphere. The frequencies to which a strong cloud response to co-condensation could be expected and its potential spatiotemporal variability over the boreal biome is further investigated using long-term measurements from SMEAR II station and UK Earth System Model (UKESM1) simulations.

2 Methods and data

This section covers the description of the main modeling tools and measurement data used in this work involving the description of the CPM utilized (Sect. 2.1), the CPM initialization and simulation setup (Sect. 2.2.), and CPM input data measurements and data processing, with independent sections dedicated to the retrievals of volatility distributions for atmospheric organics (Sect. 2.3 and subsections therein). The final section is dedicated for describing the UKESM1 simulations (Sect. 2.4).

2.1 The adiabatic cloud parcel model (PARSEC-UFO)

The base of the CPM chosen for this study is the Pseudo-Adiabatic bin-micRophySics university of Exeter Cloud parcel model (PARSEC). It was developed based on the Institute for Marine and Atmospheric research Utrecht (IMAU) pseudo-adiabatic CPM (ICPM, Roelofs and Jongen, 2004; Roelofs, 1992) to allow for simulation of both pseudo-adiabatic and adiabatic ascents of air parcels (Partridge et al., 2011, 2012) as well as numerous optimizations to reduce simulation computational costs, such as a variable time-stepping scheme option for the dynamics/microphysics. PARSEC simulates the condensation and evaporation of water vapor on aerosol particles, particle activation to cloud droplet, unstable growth, collision and coalescence between droplets, and entrainment. In all simulations performed in this study PARSEC is used in adiabatic ascent configuration and the fixed time-stepping option in PARSEC is employed.

The model can be initialized with aerosol populations consisting of one or more internal or external mixtures of sulfuric acid, ammonium bisulfate, ammonium sulfate, OA, black carbon, mineral dust and sea salt. The PNSD are presented in a moving-center binned microphysics scheme comprising 400 size bins between 2 nm and 5 μm in dry radii, which are constructed at model initialization from the three parameters describing log-normal size distributions for the i number of modes – the geometric mean diameter (D_i), the total mode number concentration (N_i), and the geometric standard deviation (σ_i). The model can be initialized with up to four log-normal aerosol modes. PARSEC further provides time evolutions of key thermodynamic and microphysical parameters e.g., the air parcel temperature (T), pressure (p), supersaturation (s), altitude (z) and the aerosol particle and hydrometeor size distributions.

The dynamical equations used in PARSEC to simulate the adiabatically ascending air parcel equations are the same to those presented by Lee and Pruppacher (1977), where the vertical parcel displacements are determined by the updraft velocity (w, set to a fixed positive constant value in the PARSEC simulations):

$$\frac{dz}{dt} = w. \tag{1}$$

202 The changes in pressure are calculated assuming hydrostatic balance and the temperature decrease along the ascent
203 follows the dry adiabatic lapse rate while also accounting for the latent heat release due to condensation:

$$-\frac{dT}{dt} = \frac{gw}{c_{p,a}} + \frac{L_e}{c_{p,a}}\frac{dx_v}{dt} + \mu_J\left[\frac{L_e}{c_{p,a}}(x_v - x_v') + (T - T')\right]w \tag{2}$$

204 where g is the acceleration of gravity, L_e the latent heat of evaporation, $c_{p,a}$ the specific heat capacity of air and x_v
205 the water vapor mixing ratio of the air parcel. μ_J is the entrainment rate describing mixing of parcel air with
206 environmental air characterized with x_v' and T'. The water vapor mixing ratio in the air parcel changes with the
207 evolving ambient supersaturation:

$$\frac{ds}{dt} = \frac{p}{\varepsilon e_s}\frac{dx_v}{dt} - (1 + s)\left[\frac{\varepsilon L_e}{R_a T^2}\frac{dT}{dt} + \frac{g}{R_a T}w\right], \tag{3}$$

208 where $\varepsilon = R_a/R_v = M_w/M_a = 0.622$ i.e., the ratio between the specific gas constants for air and water vapor,
209 respectively, or alternatively the molecular weight of water and air, respectively. e_s is the saturation vapor pressure
210 of water. To solve the ordinary differential equations (Eqs. 2–3), the time derivative of the water vapor mixing is
211 approximated as

$$\frac{dx_v}{dt} \approx -\frac{\Delta x_L}{\Delta t} - \mu_J(x_v - x_v' + x_L)w \tag{4}$$

212 where Δt is the model time step (0.1 seconds) and the liquid water mixing ratio (x_L) is calculated as a sum of the
213 liquid water mixing ratio across all the 400 size bins (index i) for each assigned mode composition (index j):

$$\Delta x_L = \frac{4\pi\rho_w}{3\rho_a}\sum_{i=1}^{n_a}\sum_{j=1}^{n_b} n_{ij}(r_{ij}^3 - r_{ij,\,dry}^3), \tag{5}$$

214 where ρ_w is density of water, ρ_a is the density of dry air, n_{ij} is the number of particles within size bin i and
215 composition j, and finally r_{ij} and $r_{ij,\,dry}$ are the wet and dry radii of the particles, respectively. The wet radii and
216 hence also the particle masses (m) change as water condenses onto the particle (indices dropped for simplicity):

$$\frac{dm}{dt} = 4\pi\rho_w r^2\frac{dr}{dt} = \frac{4\pi\rho_w r(S - S_{eq})}{\frac{\rho_w RT}{DIFF_v^* e_s} + \frac{L_e\rho_w}{kT}\left(\frac{L_e}{RT} - 1\right)}, \tag{6}$$

217 where k is the thermal conductivity of air, and $DIFF_v^*$ is size-dependent water vapor diffusivity (from Pruppacher
218 and Klett, 1997). Eq. (6) is approximated within PARSEC using a linearized form of the condensation equation
219 (Hänel, 1987). Finally, S is the ambient saturation ratio ($S = s + 1$) and S_{eq} ($S_{eq} = RH / 100\%$) the equilibrium
220 saturation ratio over the (spherical) wet particle surface, the difference of which determines the quantity of excess
221 vapor for the diffusional growth of the particle. While S depends on the updraft source and condensation sink (Eq.
222 3), S_{eq} depends on the particle wet radius and composition and it can be calculated using the Köhler equation
223 (Köhler, 1936), traditionally expressed as:

$$S_{eq} = \frac{e}{e_s} = a_w\exp\left(\frac{2M_w\gamma}{RT\rho_w r}\right) \tag{7}$$

224 where e is the partial vapor pressure of water in equilibrium, a_w the water activity, γ the droplet surface tension
225 (assumed to be that of water; see Table 1), R the universal gas constant, T the droplet temperature and r the droplet

radius. Assuming dilute droplets, Eq. 7 is approximated in PARSEC as follows for the equilibrium supersaturation ratio (Hänel, 1987):

$$S_{eq} \approx \exp\left(\frac{A}{r} - \frac{B}{\left(\frac{r}{r_{dry}}\right)^3 - 1}\right),$$ (8)

where

$$A = \frac{2M_w\gamma}{RT\rho_w}$$ (9)

and

$$B = \frac{\phi_S M_w \varepsilon_V \rho_s \nu}{M_s \rho_w}$$ (10)

A and B in Eqs. (9) and (10) are the Köhler coefficients, where M_w is the molecular weight of water (g mol^{-1}), M_s refers to the molar mass of the soluble fraction, ρ_w is the density of water (g m^{-3}), ϕ_s is the osmotic coefficient of salt in the solution ($\phi_s \approx 1$ in ideal solutions), ν is the dissociation constant, and ρ_s and ε_V are the density and the volume fraction of the soluble mass in the aerosol particle, respectively. The dissociation constant is calculated as $\nu = \left(\sum_i c_i^+ + \sum_j c_j^-\right) / \sum_{ij} c_{ij}$, where, c_i^+ and c_j^- are the concentrations of positive and negative ions and c_{ij} is the concentration (mol L^{-1}) of the electrolytes in solution. For detailed descriptions of the B term, the reader is directed to Roelofs (1992).

PARSEC has been further extended to include Köhler and condensation/evaporation equations for organic species of varying volatilities (Lowe, 2020). This extension of the model is referred to as PARSEC with the Unified Framework for Organics (PARSEC-UFO), and it is the CPM version used throughout the presented study. Within PARSEC-UFO, the volatility distributions are given using the VBS framework (Donahue et al., 2006) with q volatility bins – each assigned with a different saturation vapor concentration, C^*. The condensation/evaporation equation for organic species is described in the same manner as in Topping et al. (2013) and as shown for water vapor in Eq (6):

$$\frac{dm_q}{dt} = \frac{4\pi \rho_w r \, DIFF_g^* \left(S_q - S_{eq,q}\right) e_{s,q}}{\frac{DIFF_g^* \Delta H_{vap,q} S_{eq,q} e_{s,q} \rho_q}{\lambda T}\left(\frac{\Delta H_{vap,q}}{R_{v,q} T} - 1\right) + \rho_q R_{v,q} T}$$ (11)

where $DIFF_g^*$ is the gas phase diffusivity (see details in Topping et al., 2013 supplementary information), and λ is the heat conductivity of air. Both $DIFF_g^*$ and λ are corrected for the transition regime of condensation. $\Delta H_{vap,q}$ is the enthalpy of vaporization, $e_{s,q}$ the saturation vapor pressure, $S_{eq, q}$ the equilibrium saturation ratio and ρ_q the density of organic species in the qth volatility bin. $S_{eq, q}$ is calculated analogous to the Köhler equation (Eq. 8):

$$S_{eq, q} = a_q \exp\left(\frac{2v_q\gamma}{RTr}\right)$$ (12)

where a_q is the activity of qth volatility bin in the bulk condensed phase, which equals the molar fraction of q due to the ideal solution approach of the study, and v_q is the molar volume of q. Following the organic condensation, the Köhler B term (Eq. 10) is updated along the adiabatic ascent, which impacts S_{eq} for water and thereby its

condensation. Finally, as temperature decreases along the parcel's adiabatic ascent, the reductions in C^* are accounted for using an Arrhenius-type Clausius-Clapeyron relation:

$$C^* = C^*(T_{\text{ref}}) \exp\left(\frac{\Delta H_{\text{vap}}}{R}\left(\frac{1}{T_{\text{ref}}} - \frac{1}{T}\right)\right), \tag{13}$$

where R is the universal gas constant and T is the air parcel's ambient temperature in Kelvin, and T_{ref} is 298.15 K. The $C^*(T_{\text{ref}})$ are calculated within PARSEC-UFO using the initial conditions as reference. ΔH_{vap} remain constant throughout the simulations in this study, and are not C^*-dependent for simplicity. It should be noted that the time step of 0.1 seconds can be too high for solving Eq. (11) for the highest volatility bins. For instance, during condensation the model may encounter $m_q + \frac{dm_q}{dt} < 0$.

If this happens then the condensation step is rejected, and instead condensation happens with a temporary timestep of $dt/2$ across two iterations. This ensures non-negative m_q. We should stress, that this sub-timestep is a new feature unique to PARSEC-UFO which is different to the variable time-stepping scheme option available in PARSEC.

2.2 PARSEC-UFO initialization and simulation setup

The simulations shown within this work are performed with PARSEC-UFO with or without co-condensation. Initially, before the start of the adiabatic ascent, an initialization takes place in PARSEC-UFO. This involves the calculation of the binned wet particle number size distribution and in the case, where co-condensation is enabled, the initialization of the volatility distribution of organics. The binned wet PNSD is calculated using the parameters describing a dry log-normal PNSD (N_i, D_i, σ_i), information on aerosol chemical composition (mass fractions of chemical species), initial RH and temperature – all given as inputs for the model. When co-condensation is turned on, PARSEC-UFO takes in the summed volatility distributions (gas+particle phase i.e., $C_{g+p,q} = C_{g,q} + C_{p,q}$) – corrected for the PARSEC-UFO initialization temperature offline (Sect. 2.3) – as input. It is then assumed upon PARSEC-UFO initialization that the gas and particle phase are in equilibrium under the initialization RH. Finally, PARSEC-UFO solves partitioning coefficients for each volatility bin (ξ_q) i.e., the distribution of organic mass between gas and particle phase:

$$\xi_q \equiv \frac{C_{p,q}}{C_{p,q} + C_{g,q}}, \tag{14}$$

where the total particle phase organic mass concentration across all volatility bins is

$$C_p = \sum_q C_{p,q} = \sum_q C_{g+p,q}\, \xi_q \tag{15}$$

and the partitioning coefficients depend on C^* as follows

$$\xi_q = \frac{C_p}{C_p + C_q^*}. \tag{16}$$

Each ξ_q is solved iteratively from Equations (15–16) following absorptive partitioning theory including water (Barley et al., 2009), as it was done by Topping et al. (2013) assuming equilibrium conditions. The iterative method is possible, as $-C_p$ is constrained by the initial PNSD and the organic mass fraction, and the relative proportions of the volatility bins (volatility distribution shape) are preserved. As assuming equilibrium conditions

limits the amount of organic vapor available for co-condensation, it may also reduce the cloud response to co-condensation. Therefore, the initial organic vapor concentrations provided here can be taken as a lower limit.

Overall, 97 daytime scenarios (local time between 10:00 and 19:00) are simulated adiabatically with PARSEC-UFO. The initialization data originate from the Biogenic Aerosols – Effects on Clouds and Climate (BAECC) campaign, which took place in 2014 at the Station Measuring Ecosystem–Atmosphere Relationships (SMEAR) II in Hyytiälä, Finland (Petäjä et al., 2016). The measurements and data processing relevant to this study are described in Sect. 2.3. The configuration of PARSEC-UFO used in this study only considers the adiabatic ascent of an air parcel, without treatment of variable vertical updraft during ascent, droplet collision and coalescence or entrainment. The simulations are performed for fixed updraft velocities of 0.1 m s^{-1}, 0.3 m s^{-1}, and 1.0 m s^{-1}, with and without co-condensation. During the CPM simulation period, SMEAR II was under daytime clouds roughly 50–60% of the time (Ylivinkka et al., 2020), which were most often low level clouds motivating selection of updraft velocities. The initial atmospheric pressure and relative humidity are set to 980 hPa and 90%, respectively, in all simulation scenarios, unless otherwise stated. The PARSEC-UFO initialization temperature varies throughout the simulation set, and is taken from interpolated radiosonde data that represents the 90% initialization RH (Sect. 2.3). The selection of the 90% RH was motivated by the previous study by Crooks et al. (2018). However, we acknowledge that more work is needed to better harmonize this parameter, along with initialization pressure, to in-situ aerosol measurements. Each modelled scenario has log-normal parameters describing a bimodal aerosol size distribution form BAECC measurements and the organic mass fraction from ACSM measurements (Sect. 2.3). The rest of the mass is assumed to be ammonium sulfate, although an ion pairing method (Äijälä et al., 2017) would suggest significant contributions also from ammonium bisulfate (Table S.2).which is generally a good approximation for SMEAR II (Heikkinen et al., 2020). For the simulations performed here, BC is not included given its small (about <5%) contribution to aerosol mass from late spring to summer (Luoma, 2021). While PARSEC-UFO does not utilize κ-Köhler theory (Petters and Kreidenweis, 2008), it might be useful to know that the assumed hygroscopicity, if translated to the hygroscopicity parameter κ, would be 0.14 and 0.72 for organics and ammonium sulfate, respectively (ideal solution; median $\kappa_{tot} \approx 0.32$). The assumed overall hygroscopicity is therefore likely to be overestimated, and it would exceed κ determined for SMEAR II experimentally in previous studies (e.g., Sihto et al., 2011 suggest $\kappa = 0.18$). Due to the likely overestimation of aerosol liquid water at initial conditions, it is also likely that the amount of organic vapor available for co-condensation after PARSEC-UFO initialization is underestimated.

Table 1 contains a summary of the simulation input data along with the values used for mass accommodation coefficient, surface tension, the vaporization enthalpy and effective soluble fraction of organics as well as the number of PNSD size bins. A more comprehensive look into the input data can be found in Table S.1. The simulation output at 50 m above cloud base, discussed later in the results section of the paper (Sect. 3), is summarized in Table 2. Particles exceeding the critical radius (calculated by Köhler theory) in their wet radii are considered as cloud droplets in this work. The output data are averaged to a fixed height output grid spaced with a two-meter resolution until 200 meters above cloud base.

2.3 PARSEC-UFO input data measurements and processing

The observational data used as PARSEC-UFO input (Fig. 1) were collected during the BAECC campaign which took place in 2014 at SMEAR II station in Hyytiälä, Finland (Petäjä et al., 2016). SMEAR II is a well characterized atmospheric measurement supersite located within a boreal forest in Southern Finland (61°51'N, 24°17'E; Hari

and Kulmala, 2005). The surroundings of the measurement site are mostly forested (80% within a 5 km radius and 65% within a 50 km radius; Williams et al., 2011). The atmospheric composition measured at the site suggests strong influence of biogenic emissions on aerosol and aerosol precursor (i.e., biogenic VOCs, BVOCs) concentrations (e.g., Hakola et al., 2012; Yan et al., 2016; Allan et al., 2006; Heikkinen et al., 2021). Anthropogenic influence is pronounced when air masses arrive from heavily industrialized areas such as St Petersburg, Russia (Kulmala et al., 2000).

As PARSEC-UFO simulations are initialized at 90% RH, which is most of the time higher than that measured at ground level, an interpolated radiosonde data product from the BAECC campaign (ARM Data Center, 2014) is used to find temperatures matching 90% RH. Radio soundings are performed four times a day (Petäjä et al., 2016). Both the temperature measured near ground level (8.4 m above ground level) and the temperature corresponding to 90% RH are shown in Fig. 1c. While these temperatures show similar temporal behavior at times, also major differences exist, arising e.g., from instable temperature profiles as well as sudden changes in air masses that the interpolated data product built from sondes sent three times a day fails to capture. A well-mixed boundary layer is assumed, and therefore the dry PNSD and aerosol chemical composition are assumed suitable as such for PARSEC-UFO input.

The PNSD for the PARSEC-UFO initialization are obtained from the Differential Mobility Particle Sizer (DMPS) measurements from SMEAR II performed within the forest canopy (Aalto et al., 2001; Petäjä et al., 2016; Fig. 1a). Since PARSEC-UFO takes in the log-normal parameters that the size distribution comprises (N_i, D_i, σ_i) also the fitting of the PNSD is performed. This is done using the Hussein et al. (2005) algorithm that allows fitting 1–4 modes into the measured distributions and decides the optimal number of modes. For the BAECC data set, the optimal number would always be between three and four modes, with a higher number of modes generally yielding a better fit to the observational data as expected. Despite the optimal number of 3–4 modes, the maximum number of modes is restricted to two as the agreement between the fitted and measured distributions remained good considering the experimental uncertainties (Fig. S.1). Statistics regarding the log-normal parameters of the fitted data during BAECC are provided in Tables 1 and S.1. The bimodal PNSD fits are also calculated for the years 2012–2017. These data are used later to evaluate the frequency of times size distributions yielding high ΔCDNC appear in long-term in-situ data.

The aerosol chemical composition for PARSEC-UFO initialization are obtained from Aerosol Chemical Speciation Monitor (ACSM; Ng et al., 2011) measurements performed within the forest canopy (Heikkinen et al., 2020). The ACSM measures the non-refractory (NR) sub–micrometer particular matter (PM$_1$) chemical composition, which means that the reported composition is restricted to organics, sulfate, nitrate, chloride and ammonium. The salts measured by the instrument do not include sea salt, because it typically exists in the coarse mode and does not fully evaporate at the ACSM vaporizer temperature of 600°C. The latter reason restricts the instrument also from detecting black carbon (BC). The composition from the ACSM measurements is shown in Fig. 1b. Statistics regarding the organic mass fractions (f_{Org}) are shown in Table 2. The ACSM data are further used to derive volatility distributions similar to those utilized by Topping et al. (2013; see Sect. 2.3.1 for details). The volatility distributions derived from ACSM are termed as CJ in the following. The letter combination refers to Cappa and Jimenez (2010), the source of the volatility distribution shapes determined for different OA types. The construction of CJ distributions suitable as PARSEC-UFO input data is explained in Sect. 2.3.1.

362   The Filter Inlet for Gases and AEROsols (FIGAERO; Lopez-Hilfiker et al., 2014) coupled with a
363   chemical ionization mass spectrometer (CIMS; the coupling of these instruments hereafter referred to as
364   FIGAERO-I-CIMS), sampling above the forest canopy in a ca. 30 m tower, is used to retrieve molecular
365   composition and volatility distributions of gas- and particle-phase species during BAECC (Mohr et al., 2017,
366   2019; Schobesberger et al., 2016; Lee et al., 2018, 2020; see Sect. 2.3.2 for details). The FIGAERO-I-CIMS
367   stands as one of the very few instruments capable of performing near-simultaneous measurements of both gas and
368   particle phases. The FIGAERO inlet allows the gas phase to be sampled while aerosol particles are collected on a
369   Teflon filter, and after sufficient particle deposition time the sample is heated and the evaporated molecules are
370   measured similarly to the gas phase. The heating procedure, which typically reaches a maximum temperature of
371   around 200°C can, however, cause thermal fragmentation of molecules (Lopez-Hilfiker et al., 2015). This leads
372   to the detection of small molecular fragments, which get assigned a higher C^* than that of the parent molecule,
373   which can be seen in the FIGAERO-I-CIMS thermograms when compounds with high C^* vaporize at
374   exceptionally high temperatures. In addition to the indistinguishable isomers from any of the phases from online
375   FIGAERO-I-CIMS measurements (or any other mass spectrometer for that matter), thermal fragmentations add
376   to the uncertainty of volatility distributions retrieved from these data. The derivation of the volatility distributions
377   derived from FIGAERO-I-CIMS data (termed F distributions in the following) is explained in Sect. 2.3.2.

378

2.3.1 Volatility distributions from ACSM data (CJ distributions)

380   Previous to the development of the FIGAERO-I-CIMS, organic volatility distributions were probed only through
381   particle phase measurements (e.g., Huffman et al., 2009b), which enabled volatility constraints of relatively low
382   volatility species (Cappa and Jimenez, 2010). More precisely, these early generation OA volatility distributions
383   were obtained from e.g. Aerosol Mass Spectrometer (AMS; Canagaratna et al., 2007) measurements coupled with
384   a thermal denuder (TD; e.g., Huffman et al., 2009a, b). The TD-AMS measurements provide thermograms (mass
385   fractions remaining in the particle phase as a function of TD temperature of ca. 25–250 °C) that could be assigned
386   to individual OA components i.e., low-volatility oxygenated organic aerosol (LV-OOA), semi-volatile
387   oxygenated organic aerosol (SV-OOA), hydrocarbon-like OA (HOA) and biomass burning OA (BBOA). Cappa
388   and Jimenez (2010) then reproduced such thermograms using a kinetic evaporation model (Cappa, 2010) through
389   fitted OA volatility distributions. In this paper, volatility distributions of this kind are referred to as CJ
390   distributions.

391   To calculate the CJ distributions for the BAECC OA types, the LV-OOA, SV-OOA and primary organic
392   aerosol (POA; taken as a mix of HOA and BBOA) from the SMEAR II ACSM long-term data set are utilized
393   (Heikkinen et al., 2021). During BAECC, the organic aerosol comprised 63% LV-OOA, 32% SV-OOA and only
394   5% POA on average. Using the time-dependent mass fractions of each OA type, mass-weighted average CJ
395   volatility distributions for each of the model initialization scenarios (97 of them) are calculated. The CJ
396   distribution shapes are taken from Cappa and Jimenez (2010), and they are provided under 298.15 K.

397   As the CJ volatility distributions have been reported for 298.15 K (Cappa and Jimenez, 2010), and
398   PARSEC-UFO simulations are generally initialized at lower temperatures (Fig. 1c), accounting for the impact the
399   temperature reduction has on C^* is necessary. The relationship between temperature and C^* is accounted for using
400   the Arrhenius-type Clausius-Clapeyron relation (Eq. 13), where T is the ambient temperature in Kelvin (the

401   PARSEC-UFO initialization temperature), and T_{ref} is 298.15 K. For the relationship between ΔH_{vap} and $C^*(T_{ref})$,

402   the formulation provided in Epstein et al. (2010) is used:

$$\Delta H_{vap} = -11\log_{10}C^*(T_{ref}) + 129, \tag{17}$$

403   where ΔH_{vap} is the change in heat (enthalpy) of vaporization in kJ mol^{-1}. A lower limit of 20 kJ mol^{-1} is set to the

404   ΔH_{vap}, which is close to the ΔH_{vap} determined for formic acid (NIST Chemistry WebBook, 2022). Eq. (17) would

405   otherwise provide too low, unphysical and even negative values. The temperature adjustment (Eq. 13), does not

406   change the shape of the volatility distribution, but the volatility distribution x-axis shifts to the left. See example

407   in Fig. S.2. After the temperature adjustments, the volatility distributions are binned to ranges between $\log_{10}C^* =$

408   [-8, 3] spaced by one decade in C^*. The lower limit is reduced by two orders of magnitude ($C^*(T_{ref}) = $ [-6, 3]), but

409   the upper limit remains as the initialization temperatures did not exceed T_{ref}. The campaign average CJ volatility

410   distribution is shown with black bars in Fig. 2a. However, each simulation utilizes a unique distribution

411   constructed using the LV-OOA, SV-OOA, and POA time series.

412

413   **2.3.2 Volatility distributions from FIGAERO-I-CIMS data (F distributions)**

414   Organic aerosol volatility distributions from FIGAERO-I-CIMS measurements conducted during BAECC (Mohr

415   et al., 2017, 2019; Schobesberger et al., 2016; Lee et al., 2018, 2020) are also derived. It can be assumed that the

416   FIGAERO-I-CIMS detected most of the OA measured with the ACSM, because FIGAERO-I-CIMS is sensitive

417   to oxidized organic species, such as organic acids (Lutz et al., 2019), and most of the observed OA mass (~95%)

418   measured by the ACSM can be attributed to oxygenated organic aerosol – thought to represent organic acids

419   (Yatavelli et al., 2015). The agreement between the two measurements is supported by the comparison between

420   the daytime FIGAERO-I-CIMS particle phase signal (of identified ions) and the OA mass concentration retrieved

421   from ACSM measurements provided in Fig. S.3. While the quantification of the FIGAERO-I-CIMS

422   measurements remains challenging and therefore whilst a quantitative comparison between the concentrations is

423   uncertain, the high correlation between measurement data (Pearson $R = 0.79$) proves that the instruments generally

424   sample the same aerosol population. Notably, the PARSEC-UFO simulations use OA mass fraction (f_{org}) only

425   from the ACSM measurements. The volatility distributions are derived from FIGAERO-I-CIMS data using

426   molecular formula parameterizations derived under 300 K in Li et al. (2016):

$$\log_{10}C^*(T_{ref}) = (n_C^0 - n_C)b_C - n_O b_O - 2\frac{n_C n_O}{(n_C + n_O)}b_{CO} - n_N b_N, \tag{18}$$

427

428   where n_C^0 is a reference carbon number; b_C, b_O, and b_N are the contributions of each carbon, oxygen, and nitrogen

429   atom to the $\log_{10}C^*$, respectively; b_{CO} is a so-called carbon-oxygen non-ideality parameter (Donahue et al., 2011);

430   n_C, n_O, and n_N are the numbers of carbon, oxygen, and nitrogen atoms in the molecular formulae assigned for the

431   FIGAERO-I-CIMS data during high resolution peak fitting of the measured mass spectra. The b-values utilized

432   are listed in Li et al. (2016). In their recent work, Huang et al. (2021) derived volatility distributions from various

433   organic vapor measurements from SMEAR II. They adjusted the Li et al. (2016) parameterization for organic

434   nitrates. As shown in Isaacman–VanWertz and Aumont (2021), the utilization of the Li et al. (2016)

435   parameterization for OA rich in organic nitrates leads to biased vapor pressure estimates. Organic nitrates are

436   known to form in the boreal air as a result of nitrate radical chemistry, which is pronounced during night, along

437   with daytime oxidation of monoterpenes in the presence of nitric oxide (e.g., Yan et al., 2016; Zhang et al., 2020).

438   To account for these nitrates, Huang et al. (2021) followed the suggestions presented in Daumit et al. (2013) and

439   treated all the nitrate functional groups as hydroxyl (—OH) groups. Given that the focus of this study is on the

440   same measurement site as Huang et al. (2021), their methodology for deriving a volatility distribution from the

441   FIGAERO-I-CIMS is followed here. Once the volatility distributions are constructed using Eq. (18) for 300 K

442   (reference temperature), their adjustments to the parcel model simulation initial temperatures using Eq. (13) is

443   performed.

444   The volatilities are calculated for the 1596 ions identified by the FIGAERO-I-CIMS measurements.

445   Afterwards the signals are binned with a decadal spacing so that all the ELVOC and LVOC are summed into one

446   bin at $C^* = 10^{-4}$ μg m^{-3}. The highest volatilities reached $C^* = 10^7$ μg m^{-3}, which is therefore set as the upper limit

447   of the volatility distribution. Following from this, the volatility span is $\log_{10}C^* = [-4, 7]$. The campaign average

448   volatility distribution is shown in red bars in Fig. 2a. The average CJ distribution exhibits generally higher

449   fractions in the ELVOC region as compared to the F distribution (Fig. 2a). This mostly results from the low/non-

450   existent SVOC and IVOC concentrations in the CJ distribution. As the ELVOCs and LVOCs contain little or no

451   gas phase signals post-initialization, the F distribution used as input for PARSEC-UFO simulations uses the

452   volatility span of $\log_{10}C^* = [0, 7]$ to speed up the simulations.

453   The average F distribution shows a remarkable agreement with the organic volatility distributions from

454   the BEACHON-RoMBAS field campaign conducted at the Manitou Experimental Forest Observatory in the

455   Colorado Rocky Mountains in summer 2011 (Hunter et al., 2017, see Fig. 2a). Initially, Hunter et al. (2017)

456   derived a volatility distribution for the total atmospheric reactive carbon (other than CH_4, CO_2 and CO) using six

457   different types of measurements and assuming minimal overlap among the measured species. Here, the Hunter et

458   al. (2017) distribution is displayed in Fig. 2a after shifting it to the mean PARSEC-UFO initialization temperature

459   (280 K) using Eq. (13) and subtracting non-oxygenated VOC signals from it for comparison. The Hunter et al.

460   (2017) distribution is not used in PARSEC-UFO simulations, it is only shown for comparative purposes due to its

461   similarity with the F distributions.

462   In Figs. 2b and c, the partitioning coefficients ξ_q from the PARSEC-UFO initialization (see Sect. 2.2) are

463   compared against the partitioning suggested by the FIGAERO-I-CIMS measurements, where the C^* represent the

464   mean PARSEC-UFO initialization temperature and range from $\log_{10}C^* = [-4, 7]$. The concentrations in volatility

465   bins with $\log_{10}C^* \leq 1$ agree, suggesting that the majority of the organics in these bins are in the particle phase.

466   Similarly, the agreement in the highest volatility bin ($\log_{10}C^* = 7$) suggests the presence of gas-phase compounds

467   only in both distributions. The estimations of the gas phase vary between $\log_{10}C^* = [1, 7]$, showing a higher gas-

468   phase fraction for the modelled partitioning coefficients (Fig. 2b–d). This variability can result from numerous

469   reasons, which apart from uncertainties related to measurements and parametrizations include viscous particle

470   coatings inhibiting equilibration between gas and particle phases, and therefore showing high particle-phase

471   concentrations of high-volatility compounds in the observations. Alternatively, these concentrations can also

472   result from thermal decomposition of lower volatility products during the FIGAERO-I-CIMS heating process

473   (Lopez-Hilfiker et al., 2015) or from the tendency of the Eq. (18) parameterization to underestimate the volatility

474   of organic nitrates (Graham et al., 2022; despite treating the –NO_3 groups at –OH groups), shown to be abundant

475   in the BAECC FIGAERO-I-CIMS data set (Fig. 2e). Understanding these differences is important and requires

476   further analysis.

477   The molecular composition of the gas-phase compounds detected by the I-CIMS during BAECC are

478 analyzed and presented in detail in Lee et al. (2018). In the following, the average composition of each volatility

479 bin during daytime is briefly described. Except for the highest volatility bin, nitrogen-containing species (CHON),

480 which are prominently organic nitrates at SMEAR II (Huang et al., 2021), make up significant mass fractions of

481 each bin in the gas phase (Fig. 2e). Fig. 2f shows the concentration of the gas-phase compounds as a function of

482 the compound carbon and oxygen atom numbers. The figure shows how ELVOCs and LVOCs have the highest

483 numbers of both carbon and oxygen atoms. IVOCs and SVOCs comprise compounds with highly variable carbon

484 skeleton lengths, but the number of oxygen atoms per compound remains low, notably always lowest for IVOCs

485 and VOCs. Formic acid (HCOOH) makes up most of the gas phase signal. It is distributed in the most volatile

486 volatility bin ($C^* = 10^7 \ \mu g \ m^{-3}$). HCOOH is one of the most abundant carboxylic acids in the atmosphere and rain

487 water (e.g., Galloway et al., 1982; Millet et al., 2015 and references therein) and is known to have various sources

488 and precursors (Millet et al., 2015). The I-CIMS measurements discussed here were also performed as part of an

489 eddy covariance flux measurement setup during BAECC (Schobesberger et al., 2016). These flux measurements

490 provided insight into the high HCOOH concentrations possibly due to high emissions from the boreal forest

491 ecosystem. More details from these results can be found in Schobesberger et al. (2016).

492

493 **2.4 UK Earth System Model (UKESM1) simulations**

494 To evaluate the frequency of times size distributions yielding high ΔCDNC (which is the percent-change in CDNC

495 due to co-condensation) during BAECC would become evident over the boreal biome in an ESM if a

496 parameterization of co-condensation was implemented, the United Kingdom Earth System Model (UKESM1,

497 Sellar et al., 2019; Mulcahy et al., 2020) is utilized. The simulations performed with UKESM1 are configured for

498 Atmospheric Model Intercomparison Project (AMIP) style simulations, where UKESM1 is run in its atmosphere-

499 only configuration with time-evolving sea surface temperature and sea ice as well as prescribed marine biogenic

500 emissions from fully coupled model simulations. In addition to the HadGEM3-GC3.1 core physical dynamical

501 model of the atmosphere, land, ocean and sea ice systems (Ridley et al., 2018; Storkey et al., 2018; Walters et al.,

502 2017), UKESM1 also contains additional component models for atmospheric chemistry and ocean and terrestrial

503 biogeochemistry for carbon and nitrogen cycle representation. The version of UKESM1 used includes

504 developments to the droplet activation scheme from Mulcahy et al. (2020) to facilitate more consistent

505 comparisons against PARSEC-UFO. In the standard configuration of UKESM1, aerosol particles are activated

506 into cloud droplets using the droplet activation parameterization of Abdul-Razzak and Ghan (2000). An alternative

507 optional configuration of UKESM1 was employed that uses the Barahona et al. (2010) droplet activation

508 parameterization, which has been shown to be more consistent when compared against an adiabatic cloud parcel

509 model over a range of conditions (Simpson et al., 2014; Partridge et al., 2015). Furthermore, in the standard

510 configuration of UKESM1, the droplet activation scheme uses the distribution of sub-grid variability of updraft

511 velocities according to West et al. (2014) with updates as described in Mulcahy et al. (2018). To facilitate more

512 consistent comparisons against PARSEC-UFO simulations that calculate droplet number using a single average

513 updraft velocity, the single characteristic updraft velocity (Peng et al., 2005) was used to initialize the droplet

514 activation scheme in UKESM1.

515   A N96L85 horizontal resolution structure (1.875°× 1.25° longitude–latitude, which corresponds roughly

516 a horizontal resolution of 135 km) is chosen for the simulations and the vertical space is split to 85 levels (50

levels between 0 and 18 km and 35 levels between 18 and 85 km). In this study the model is run in a nudged configuration (horizontal wind nudging (but not temperature) between model levels 12 and 80 with a constant 6-hour relaxation time), for the years 2009–2013 inclusively. External forcing and emission datasets are consistent with the Coupled Model Intercomparison Project Phase 6 (CMIP6) implementation as described in Sellar et al. (2020). The simulation setup is same as in the Aerosol Comparisons between Observations and Models (AeroCom) Phase III GCM Trajectory experiment (AeroCom, 2022; Kim et al., 2020).

The UKESM1 aerosol scheme represents the particle size distributions with five log-normal modes: the nucleation soluble mode, Aitken soluble and insoluble modes, accumulation soluble mode, and coarse soluble mode (Mulcahy et al., 2020). The aerosol microphysical processes of new particle formation (NPF), condensation, coagulation, wet scavenging, dry deposition and cloud processing are handled with GLOMAP (Global Model of Aerosol Processes; Mann et al., 2010; Mulcahy et al., 2020). The UKESM1 NPF mechanism follows the parameterization derived in Vehkamäki et al. (2002) for binary homogeneous nucleation of H_2SO_4 and water. Separate boundary layer NPF is not included in the simulations (Mulcahy et al., 2020). The soluble aerosol size distribution lognormal aerosol modal parameters (nucleation mode, soluble Aitken mode and soluble accumulation mode) and sub-grid scale updraft velocities with a 3-hour time resolution at cloud base of stratiform clouds are used. These diagnostics are subsequently masked to include only data in which activated aerosol particles exceeds zero and the temperature exceeds 237.15 K in keeping with criteria used by the droplet activation scheme. The PNSD modal parameters are used to construct aerosol size distributions. In UKESM1 the geometric standard deviations are fixed parameters. The same values are used for consistency for the modes that are accounted for in this work. The geometric standard deviation for UKESM1 Nucleation soluble mode and the Aitken soluble mode is 1.59, and for the accumulation soluble mode it is 1.40. UKESM1 outputs for the Aitken insoluble mode and coarse mode are not used in analysis performed in this study because they do not contribute to CCN in the model representation of cloud droplet activation. UKESM1 uses a 26% SOA yield from monoterpenes, the emissions of which are from The Model of Emissions of Gases and Aerosols from Nature (MEGAN) version 2.1 (Guenther et al., 1995) .

3 Results and discussion

3.1 Organic condensation: time and volatility dependencies

The first PARSEC-UFO simulation results (Fig. 3) correspond to initializing the model with data collected on May 11, 2014 at 13:37 EET (East European winter time). This simulation is identified from the full dataset as one that represents a median cloud response to co-condensation of organics and water. Figure 3a shows the vertical evolution of total SVOC and IVOC concentrations in the gas phase for the three different updraft scenarios (w = 0.1, 0.3, or 1 m s^{-1}, respectively). Both SVOC and IVOC concentrations decrease significantly along the adiabatic ascent in subsaturated conditions below cloud base (CB). Given that the PARSEC-UFO simulation output is saved with 2-meter vertical resolution, "below CB" contains all the simulation output under subsaturated conditions, and the RH at CB is defined as min(RH ≥ 100 %). Both SVOC and IVOC concentrations decrease significantly along the adiabatic ascent in subsaturated conditions below cloud base (CB, RH$_{CB}$ = 100%). "Below CB" is defined as the ascent from RH = 90% upwards as long as RH < 100%. Given that the PARSEC-UFO simulation output is saved with 2-meter vertical resolution, "below CB" contains all the simulation output under sub-saturated conditions. When moving to saturated conditions, SVOCs and IVOCs are scavenged. This result is in line with

556 Bardakov et al. (2020), who modelled complete gas removal of volatility bins up to roughly $\log_{10}C^* = 9$ within

557 convective clouds.

558   When considering all 97 simulations, the net mass fractions of organics condensed below CB are on

559 average 91, 70 and 28% for the 0.1, 0.3 and 1.0 m s^{-1} updraft, respectively, which in absolute concentrations means

560 additions of 1.8, 1.4, and 0.7 μg m^{-3} to the aerosol particle soluble mass (Table 2). The yielded mass concentrations

561 are in the same order of magnitude as the PM$_1$ mass concentrations measured during BAECC (interquartile range,

562 IQR: 0.95, 1.95, and 3.22 μg m^{-3} from ACSM data), which means that such organic condensation along the

563 adiabatic ascents as simulated here would yield roughly a doubling of the soluble mass due to SVOC and IVOC

564 condensation below CB. Figures 4d–f show the simulated organic condensate concentrations for each volatility

565 bin. While the condensed fraction for the highest volatility bin is smallest (Figs. 4a–c), the absolute concentrations

566 of condensate are amongst the largest due to the high availability of organic vapor in the highest volatility bin

567 (mostly HCOOH; Sect. 2.3.2). The condensation efficiency of the highest volatility bin correlates with the number

568 of large particles serving as condensation sink for vapors (Fig. S.4). This suggests that these organic vapors are

569 likely to condense onto larger particles, which are susceptible to be activated into cloud droplets regardless of co-

570 condensation. Similar correlations are observed to a lesser extent with the $\log_{10}C^* = 6$ volatility bin (not shown).

571 In this work, the information of the size ranges of particles which the high-volatility IVOCs condense onto is

572 lacking. Therefore, more systematic studies should be conducted to better understand whether the condensation

573 of the high-volatility IVOCs onto ultrafine particles is sufficient enough to lead to increased droplet activation.

574   The exact numbers presented here should, however, be assessed with caution as an ideal liquid phase, as

575 well as partitioning being determined by mole fractions of water-soluble organics are assumed (Sect. 2.1.1).

576 Topping et al. (2013) looked into the assumption of ideality in their supplementary material. They found it to

577 enhance the amount of modelled organic condensate as compared to a non-ideal case. However, their simulations

578 exploring non-ideality with organic activity coefficients predicted with the UNIFAC method (UNIQUAC

579 Functional-group Activity Coefficients; Fredenslund et al., 1975) still led to significant amounts of condensed

580 organic mass. The impact of the ideality assumption was shown to be most significant in their highest volatility

581 bin ($C^* = 1000$ μg m^{-3}). Activity coefficients (and solubilities) of organics should in the future be better constrained

582 to assess the impact on volatility bins of $\log_{10}C^* > 3$, which was not explored in Topping et al. (2013). As discussed

583 in the Topping et al. (2013) supplementary information, it is likely that solubility decreases towards the higher

584 volatility bins. Here, a simple assessment of the assumption of ideality (Appendix A, Fig. A.2b) suggests that the

585 gained organic soluble mass reduces only when the overall mass accommodation coefficient for organics is less

586 than 0.4. This would mean that the organic condensation shown here could be taken as the upper limit.

587   Further investigation on how efficiently different volatility bins condensed along the adiabatic ascents

588 across all the 97 simulation scenarios repeated with the three fixed updraft velocities is also performed (Fig. 4a–

589 c). In the 0.1 m s^{-1} updraft scenario, almost all organic vapor condenses up to $\log_{10}C^* = 5$ and the condensation

590 capability of the highest volatility bin ($\log_{10}C^* = 7$) shows the highest variability (~20–91% condensed below CB;

591 Fig. 4a). The same features can be observed with the 0.3 m s^{-1} and 1.0 m s^{-1} updraft simulations, although the

592 fraction of organic vapor condensed per volatility bin is reduced (in the $w = 1$ m s^{-1} scenarios only ca. 30% of the

593 vapor condenses below CB (Figs. 4b–c). The results from these simulations reveal that there is enough time only

594 under slow adiabatic ascents for most of the organic vapor to condense.

595

3.2 Impact of meteorological conditions on the sensitivity of cloud microphysics to organic vapor condensation

As explained previously in Topping et al. (2013), the CDNC enhancements associated with co-condensation arise from the increase in organic solute concentration, which decreases the critical supersaturation (s^*) needed for a given particle to activate. The s^* is reduced about 10–20% for the May 11, 2014 at 13:37 EET case presented in Fig. 3b when co-condensation is enabled. This reduction is calculated for a particle with a dry radius of 71.9 nm (i.e., the smallest activated dry radius when co-condensation is disabled, r^*_{noCC}). Fig. S.5 shows the development of the wet particle size as a function of altitude in the PARSEC-UFO simulation summarized in Fig. 3. It clearly demonstrates the differences introduced by co-condensation through the activation of new size bins (4 size bins in total when $w = 0.1$ m s^{-1}) that would have remained as interstitial aerosol particles in the simulations where co-condensation is turned off. The enhanced growth of more particles due to co-condensation enhances the water vapor condensation sink, which leads to a reduction in the achieved maximum ambient supersaturations (s_{max}; see Fig. 3c for the May 11 case and Table 2 summarizing all the 97 simulations). As the meteorological conditions are the same in simulations performed with and without co-condensation, the condensation sink dictates the changes in s_{max} (Eq. 3). A reduced s_{max} would typically lower the number of aerosol particles activating into cloud droplets, but here the reductions in s^* are greater than the reductions in s_{max}, which therefore leads to an enhanced CDNC (see Fig. 3b–c for the May 11 case). This can be interpreted as a competition effect between the s_{max} and s^* reductions, respectively, which the s^* reduction wins. When examining the 0.1 m s^{-1} updraft case in the May 11$^{\text{th}}$ simulation shown in Fig. 3, the s_{max} is reduced ~7%, which is less significant than the s^* reduction of ~20%. This leads to a 22% enhancement in CDNC (Fig. 3d) as r^* reduces from 72 nm to 66 nm ($\Delta r^* \approx 6$ nm). Fig. 3e shows the droplet spectrum for the May 11 case, which highlights the consistent shift of droplet sizes to smaller diameters due to organic co-condensation (see also Fig. S.5, which displays the same May 11$^{\text{th}}$ simulation with $w = 0.1$ m s^{-1}). The impact such shift could have on cloud lifetime and precipitation should be studied further.

The modelled BAECC campaign median CDNC values (over the 97 simulations) without co-condensation are on average 161, 300 and 530 cm^{-3} in modeling scenarios utilizing 0.1 m s^{-1}, 0.3 m s^{-1}, and 1.0 m s^{-1} updrafts, respectively (Table 2). CDNC is shown to correlate well with the accumulation mode number concentration (N_2), and at times with the Aitken mode number concentration (N_1) if the Aitken mode particles are large enough in size and accompanied with strong enough updrafts and a low N_2 (Fig. S.6). The reductions in the smallest activated dry radii due to co-condensation ($r^*_{\text{noCC}} - r^*_{\text{CC}}$) are on average ~8, ~7, and ~5 nm for the modeling scenarios utilizing 0.1 m s^{-1}, 0.3 m s^{-1}, and 1.0 m s^{-1} updrafts, respectively, and the corresponding median ΔCDNC are ~16, ~23 and ~19%, respectively (Table 2 and Fig. 5a). The swarm plot on Fig. 5a shows that ΔCDNC and CDNC do not correlate i.e., low CDNC in the noCC runs does not favor high ΔCDNC.

On average during the BAECC simulation period (97 simulations), the highest ΔCDNC are found when initializing the model with a 0.3 m s^{-1} updraft velocity (also visible in Fig. 3d for the May 11 case) followed by ΔCDNC predictions for the 1 m s^{-1} case. In the latter, high supersaturations are achieved leading to the formation of many cloud droplets, yet the effects of co-condensation remained less pronounced as the high ascent speed poses kinetic limitations for organic condensation (see Sect. 3.1 and Fig. 4). Despite the highest organic uptake in the 0.1 m s^{-1} updraft simulations (Fig. 4a, d), the ΔCDNC remains the lowest. This can be explained by the low s_{max}, which remains insufficient to activate small particles to cloud droplets (r^*_{noCC} ~64 nm; Table 2). As the Aitken mode possesses most particles in terms of number (Table 1), the few nm reductions in r^* affect ΔCDNC

the most when the r^* reduction takes place on the steep PNSD slopes (high $d/d\log_{10}D$ ~~$(dN/d\log_{10}D)$~~~~dN/dD~~) between

the Aitken and accumulation mode. When the updraft velocity is low (0.1 m s^{-1}), the r^* are too large to overlap

with the parts of the PNSD with a high ~~dN/dD~~slope even if r^* reduces greatly due to co-condensation. Due to the

high updraft-dependency of the modelled ΔCDNC, future process modeling work should consider performing

simulations following updraft probability density functions (PDF), as used in GCMs, and calculating PDF

weighted CDNC (West et al., 2014). This way more weight will be given to lower updrafts, and the model outputs

will be more robust since the air parcels do not experience single updrafts in reality.

Besides updraft velocity, the modeled ΔCDNC are also affected by PARSEC-UFO initialization

temperatures. This can be seen when the effect of the volatility distribution upgrade (from CJ to F) on the modelled

ΔCDNC is investigated. For this purpose, an additional set of PARSEC-UFO simulations using the CJ volatility

distribution are performed. ~~Perhaps surprisingly, the~~The CDNC enhancements due to co-condensation attained

with the CJ volatility distribution are negligible (median ΔCDNC is 0; Fig. S.7) and therefore strikingly different

from those presented in Topping et al. (2013). The large difference in the modeled ΔCDNC between the F and CJ

simulations arises from the low amount of organic vapor available for condensation ($\sum C_g^{INIT}$ is only 0.10 µg m^{-3}

in CJ simulations while in the F simulations it is 2.05 µg m^{-3}), which in turn results from the low PARSEC-UFO

initialization temperature attained from the radio soundings (Sect. 2.3). If the initialization temperatures were

higher, more organic vapor would remain in the gas phase after PARSEC-UFO initialization, and larger ΔCDNC

could be modeled. The simulations performed in Topping et al. (2013) were initialized at 298 K, which explains

why they report significant CDNC enhancements due to co-condensation using a similar CJ volatility distribution

as used here. We can reproduce the Topping et al. (2013) findings when increasing the initialization temperature

with PARSEC-UFO (see Fig. S.8) and also demonstrate that by decreasing the initialization temperature from 298

to 280 K (the BAECC median temperature), the ΔCDNC modeled by Topping et al. (2013) should also be

negligible (Fig. S.8). These findings emphasize the critical role of the initialization temperature (and assumptions

made on equilibrium upon model initialization) that impacts the amount of organic vapor present in the gas phase

prior to the air parcel's ascent. Additionally, the result suggests high importance of organic vapors with saturation

vapor concentrations exceeding $\log_{10}C^* = 3$ (under 298 K) for co-condensation. If one were to utilize CJ

distributions in future co-condensation work, one could consider multiplying the highest volatility bins e.g., with

a carefully selected constant. Similar approaches have been used previously when modeling SOA formation from

IVOCs (Lu et al., 2018).

As the results from Fig. 4 underline the time-dependence of co-condensation (Sect. 3.1), it is worth

remembering that the PARSEC-UFO initialization RH is set to 90% where equilibrium conditions are assumed

(see Sects. 2.4 and 2.2). Therefore, the kinetic effects play a role only from 90% to 100% RH. Importantly, if the

initial RH was set to a lower value, more time would be available for co-condensation before reaching CB, and if

the initial RH was set to a higher value, less time would be available. On the other hand, due to the assumption of

initial equilibrium conditions, a lower initial RH also ensures a higher organic vapor concentration available for

co-condensation, and a higher initial RH reduces the organic vapor availability. Together with initial temperature,

the initial RH strongly control the amount of organic vapor available for co-condensation (Appendix A, Fig. A.1,

Fig. S.3) and thereby the amount of soluble organic mass yielded by the time the air parcel reaches cloud base.

While the decision of maintaining a fixed initial RH for the different simulations is proven useful for this study

as it eases the data interpretation process, it should be acknowledged that the initial RH could be better constrained

676 in future simulations. Naturally, the organic vapor condensation depends on the initial RH, and as a result ΔCDNC
677 is also sensitive to the selection of the initial RH (Fig. A.1). If the initial RH is set to 60%, CDNC enhancements
678 as high as ~100% could be expected, while if the initial RH is set to 99% the enhancements are expected to range
679 between 0 and ~20%. This variation is greater than the impact the ideality assumption (or the selection of
680 vaporization enthalpy) has on ΔCDNC (Sect. 3.1, Appendix A).

681

3.3 Impact of initial aerosol size distribution and organic vapor concentration on the sensitivity of CDNC
to organic vapor condensation

685 As briefly mentioned in the previous section, PNSD affects ΔCDNC along with the initial meteorological
686 conditions. The importance of Aitken mode in ΔCDNC associated with turning co-condensation on in PARSEC-
687 UFO is exemplified in Fig. 5b for the 0.3 m s^{-1} updraft simulations. In this figure, the initial dry PNSD are averaged
688 from the simulations with the highest 25% and lowest 50% modelled ΔCDNC, respectively. The PNSD
689 corresponding to the highest 25% of the modelled ΔCDNC has a very minor accumulation mode and a large
690 Aitken mode (with respect to the mode total number concentrations i.e., N_2 and N_1, respectively) with a diameter
691 (D_1) of ~40 nm (D_2 is ~110 nm). It is named as PNSD$_{NUM}$, where NUM refers to a strong nascent ultrafine mode
692 characteristic of the shown size distribution. ~The PNSD$_{NUM}$ gain the highest ΔCDNC despite a relatively small
693 change in the smallest activated dry radii, because of the steep PNSD slope in the size-range where the smallest
694 activated dry radii reduce (Fig. S.9). The slope compensates for a comparatively small reduction in the smallest
695 activated dry radii by sharply increasing the number of particles that activate, when co-condensation is enabled.
696 The PNSD corresponding to the lowest 50% of the modelled ΔCDNC is strongly bimodal, where the Aitken and
697 accumulation modes are almost equal in terms of N. Moreover, the two modes are separated by a clear Hoppel
698 minimum (Hoppel and Frick, 1990). Hoppel minimum is characteristic for aerosol populations, which have
699 undergone cloud processing. The PNSD associated with the lowest ΔCDNC tend to have the smallest activated
700 dry radii close to the Hoppel minimum, where the PNSD slope is negligible (Fig. S.10). Therefore, the integral
701 through this range provides less particles to be activated to cloud droplets, and the ΔCDNC remain low. It should
702 be noted, however, that the reductions in the smallest activated dry radii are on average higher in the simulations
703 initialized with PNSD$_{NUM}$ (Fig. S.11a) due to higher availability of organic vapors (Fig. S.11b) and their
704 condensation to a more critical size range. Nonetheless, it is evident that the shape of the PNSD dictates the
705 magnitude of the ΔCDNC, as a ~4 nm reduction in the smallest activated dry radius can lead to a CDNC
706 enhancement of ~45% in the case of a PNSD$_{NUM}$, while in the case of a PNSD with a Hoppel minimum, ΔCDNC
707 would be only ~10% (Fig. S.11). These~is results~ underlines~ that environments rich in particles from a local source
708 would be more susceptible to high ΔCDNC due to co-condensation while regions with aged and cloud processed
709 size distributions are affected less (here, ΔCDNC<20% in our simulations; Fig. 5a).
710 Interestingly, a PNSD$_{NUM}$ nascent ultrafine aerosol particle mode (NUM) was found to be important
711 when looking into suitable conditions for large increase in CDNC caused by surface active organics (Ovadnevaite
712 et al., 2017; Lowe et al., 2019). Lowe et al. (2019) utilized a similar CPM (ICPM, Sect. 2.1) as used in this study
713 (notably without co-condensation), but enabled a fraction of the particulate organics to form a thin, max. 0.2 nm
714 thick film around the particle. The film was characterized by a surface tension of 40 mN m^{-1} as opposed to the
715 surface tension of pure water (72.8 mN m^{-1}). The idea of this compressed film (CF) approach was to simulate the
716 surface tension reductions caused by organic species leading to the activation of smaller particles to cloud droplets

at the coastal Mace Head site (Ovadnevaite et al., 2017). Through sensitivity studies, Lowe et al. (2019) found that the largest percent change in CDNC due to surface active organics (>10%) took place in Mace Head when $N_2 < a N_1^b + c$ ($a = 602$, $b = 0.0884$, $c = -766$). The increase in CDNC in the Lowe et al. (2019) study was also attributed to the reduction in s^* when comparing against simulations where the surface tension was that of water. Moreover, the same competition effect between s_{max} and s^* reductions – as described here in Sect. 3.2 – was demonstrated in their study, but just triggered by different chemical parameters. The sensitivity of the CDNC enhancements to $PNSD_{NUM}$ in this study as well as in Lowe et al. (2019) demonstrates that the activation of fresh and non-cloud-processed aerosol particles is susceptible to small reductions in s^* that can be triggered e.g., by organic surfactants or co-condensation. Importantly, potential surface activity also affects the CCN activation behavior of atmospheric organics (Ruehl et al., 2012, 2016; Lowe et al., 2019), correlating with volatility and solubility. The combined effect of all these three properties needs to be thoroughly investigated in the future.

In conjunction with the ΔCDNC susceptibility to $PNSD_{NUM}$, this study most critically highlights the importance of incorporating multimodal, and representative size distributions in process modeling studies examining the cloud response to co-condensation (or surface-active organics as demonstrated in Lowe et al., 2019). Topping et al. (2013), for example, used monomodal distributions (with varying log-normal parameters) in their study, which could lead to overestimation of ΔCDNC as size distributions with Hoppel minima are not explored. Multimodal distributions were used later by Crooks et al. (2018), but further explanation of the cloud response of the update remained lacking. In summary, our results together with the Lowe et al. (2019) results suggest that in clean environments with a local source of ultrafine particles, such as the boreal forest or marine environments, organic species in the presence of a NUM-featured PNSD can have significant impact on cloud properties either via co-condensation or through surface tension reductions.

Subsequently, a dry PNSD-based criteria for identifying regimes (conditions) in which co-condensation has the highest impact on CDNC are defined. It is found that restricting the ratio between the accumulation and Aitken mode geometric mean diameters in the initial dry PNSD to below six (i.e., $D_2/D_1 < 6$) and the Aitken mode number concentration to exceed 1000 cm^{-3} (i.e., $N_1 > 1000$ cm^{-3}) would yield ΔCDNC >20% in our simulations (Fig. 5d). By using the diameter ratio criterion, size distributions without a distinguishable Hoppel minimum are selected, which is characteristic in the simulations yielding the highest ΔCDNC (Fig. 5b) and the high N_1 ensures a high concentration of aerosol particles potentially activating into cloud droplets.

In addition to the $PNSD_{NUM}$ features, also the initial organic vapor concentration (C_g^{INIT}) influences the modeled ΔCDNC. The extent to which the modeled ΔCDNC are sensitive to C_g^{INIT} is depicted in Fig. 5c using the PARSEC-UFO simulations performed with 0.3 m s^{-1} updrafts. The y–axis represents the modeled ΔCDNC and the x-axis the organic vapor concentration distributed in $\log_{10} C^*$ bins within [-4, 4] (denoted as $C_{g, -4:4}^{INIT}$) i.e., in bins that do not show high dependency on the available surface area (see Sect. 3.2 and Fig. S.4 for details). The relationship is not straightforward, but linear increases in ΔCDNC as a function of $C_{g, -4:4}^{INIT}$ can be seen under constant, yet sufficiently high s_{max} (here >0.2%). Under the modelled scenarios, where $s_{max} > 0.2\%$ the $C_{g, -4:4}^{INIT}$ is generally low (< 2 μg m^{-3}). Still, the highest CDNC enhancements during the BAECC simulation period are achieved under these conditions. The high CDNC enhancements can be achieved – despite the low organic vapor abundance simply because the soluble organic mass is distributed to more smaller particles. The markers in Fig. 5c are color-coded by the initial PNSD surface area, which under a constant updraft anticorrelates with s_{max} (see

Eq. 3). ΔCDNC shows high sensitivity to $C_{g,-4:4}^{INIT}$ when the dry PNSD surface area stays below a 100 μm^2 cm^{-3} threshold. Based on this analysis, it can be concluded that in the presence of a NUM-featured PNSD enabling the formation of high supersaturations (the dry PNSD surface area stays below 100 μm^2 cm^{-3}), an adiabatic ascent with an updraft of 0.1 or 0.3 m s^{-1} can yield ΔCDNC of >40% if 1 μg m^{-3} of co-condensable organic vapor is present in the rising air. This is a likely occurrence in the spring and summertime boreal forest (Huang et al., 2021). However, it should be noted that under such scenarios the modeled ΔCDNC are highly sensitive to organic vapor concentration (Fig. 5c) and a reduction of ~0.5 ug m^{-3} in organic vapor concentration can half the modeled CDNC when the PNSD surface area is low. The simulations performed with the highest updraft velocity ($w = 1.0$ m s^{-1}) yield lower ΔCDNC under these clean conditions (ΔCDNC does not exceed 40%) even though the simulated s_{max} increase as opposed to the results obtained with lower updrafts (e.g., Table 2), because of the kinetic limitations hindering co-condensation (see Sect. 3.1).

3.4 Expected seasonality in the impact of co-condensation on CDNC at SMEAR II

In the following, the seasonality of the dry PNSD surface area at SMEAR II (6-year-long time series, 2012–2017) is investigated to estimate how often it stays below the previously mentioned threshold of 100 μm^2 cm^{-3} i.e., times when only 1 μg m^{-3} of co-condensable organic vapor present in the rising air could yield significant ΔCDNC. This is followed by an investigation of the frequency of the PNSD criteria (D_2/D_1<6 and N_1>1000 cm^{-3}) fulfillments in the long-term size distribution measurements at SMEAR II.

Fig. 6a shows the seasonality of the dry surface area at SMEAR II. During daytime (9–19 EET) the surface area stays below the previously mentioned threshold 86% of the time during the 2012–2017 measurement period (Fig. S.12), which suggests that under 0.3 m s^{-1} updraft velocities, generation of s_{max}>0.2% at this site is likely. During summer months, the likelihood of surpassing the dry PNSD surface area threshold of 100 μm^2 cm^{-3} increases from 10% to 22% (Fig. S.12) due to biogenic SOA formation (e.g., Tunved et al., 2006; Heikkinen et al., 2020), which grows the accumulation mode in the PNSD. Biogenic SOA formation depends on the SOA precursor i.e., BVOC emissions and concentrations. Monoterpene concentrations are highest at SMEAR II in summer (Kontkanen et al., 2016; Hakola et al., 2012) as their emissions are strongly temperature-driven (Guenther et al., 1993). The organic vapor concentration available for co-condensation is therefore also highest in summer, but due to the enhanced surface area, the soluble organic mass is distributed to larger particles dampening the cloud response to co-condensation. However, the monoterpene emission period is longer than just summer, and elevated monoterpene concentrations can be observed throughout the thermal growing season (when the daily average temperature is above 5°C; Kontkanen et al., 2016; Hakola et al., 2012). Therefore, monoterpene emissions take place also at times when the dry PNSD surface area stays below the 100 μm^2 cm^{-3} threshold.

Fig. 6b shows the dry PNSD surface area derived from the long-term PNSD measurements at SMEAR II as a function of temperature. When the ambient temperature exceeds 5°C, the dry PNSD surface area starts to increase with increasing temperature. The dry PNSD surface areas and ambient temperatures (from 8.4 m height; Fig. 1c) from the BAECC simulation period are also shown to highlight the fact that the BAECC sample represents well the long-term statistics of the thermal growing season, providing confidence in the representativity of the BAECC sampling period for this boreal environment. The BAECC samples are color-coded by the modelled ΔCDNC. The highest ΔCDNC (i.e., ΔCDNC > 40%) are modeled when the dry PNSD surface areas are below the 100 μm^2 cm^{-3} threshold. Importantly, most of these model scenarios yielding ΔCDNC > 40% coincide with

ambient temperatures between 5 and 8°C i.e., at times when the monoterpene concentrations are not at their highest yet sufficient concentrations of organic vapor are still present to cause a large cloud response. It can thereby be concluded that the highest ΔCDNC due to co-condensation can be expected in thermal Spring and Fall. However, due to the seasonality in hygroscopicity and the slightly higher κ in spring and autumn (as opposed to summer; Fig. 6a) the likelihoods of obtaining s_{max} exceeding 0.2% to yield significant ΔCDNC can be somewhat buffered due to hygroscopic growth.

Next, the frequency to which the PNSD criteria ($D_2/D_1<6$ and $N_1>1000$ cm^{-3}) are fulfilled in the long-term size distribution measurements is examined. For this purpose, the same 6-year PNSD data set collected at SMEAR II fitted with two log-normal size distributions (Hussein et al., 2005) is utilized. The percentage of times the criteria are met is shown in Fig. 7a. The highest frequencies (30–40% of the time) are observed in April, May and September, which correlates with a high new particle formation (NPF) frequency at the site (Nieminen et al., 2014; Dada et al., 2017). The monthly median size distributions fulfilling the criteria are shown in Fig. 7c. They all clearly exhibit the lack of a Hoppel minimum, similarly to PNSD$_{NUM}$, and suggest a potentially high impact of newly formed particles on cloud properties through co-condensation. However, future work should focus on understanding how frequently the measured PNSD$_{NUM}$ are actually exposed to droplet activation, which would help us assess the likelihood of large CDNC enhancements taking place in reality. This is particularly important, because NPF typically takes place in sunny, non-cloudy days, which provides time for the PNSD$_{NUM}$ to evolve before exposed to cloud base and subsequent droplet activation. The results again clearly emphasize the need of accurate representation of aerosol size distributions and lifecycle in models (such as other CPMs or global circulation models, GCMs) to account for the impacts of co-condensation and the strong seasonality to be expected in the magnitudes in ΔCDNC.

3.5 Expected spatiotemporal variability in the impact of co-condensation on CDNC over the boreal biome

In this section the SMEAR II results are compared against a 5-year UKESM1 simulation (see Sect. 2.4; analysis restricted to the boreal biome). While the SMEAR II PNSD data are retrieved at ground level, utilization of the UKESM1 modal parameters (only soluble modes considered) from CB is chosen, because these PNSD log-normal parameters would actually meet the cloud droplet activation scheme in the model. Previous co-condensation parameterization schemes have also been developed to treat the CB PNSD to account for co-condensation (Connolly et al., 2014; Crooks et al., 2018). The monthly averages of the percentage of times the criteria ($D_2/D_1<6$ and $N_1>1000$ cm^{-3}) are fulfilled in the boreal grids are shown in Fig. 7b. Here, the Aitken mode geometric mean diameter and total number concentration (D_1, N_1) and accumulation mode geometric mean diameter (D_2) are obtained from the soluble Aitken and accumulation modal parameters (see Sect. 2.4 for more details regarding the UKESM1 modes). The frequencies, which remain roughly well below 6%, are in general much lower than observed at SMEAR II. This can be explained by the lack of the boundary layer NPF process in the UKESM1 simulations (Sect 2.4). Therefore, the UKESM1 results can be taken as the lower estimate. Fig. 7d displays the monthly median PNSD in the boreal grid cells fulfilling the criteria ($D_2/D_1<6$ and $N_1>1000$ cm^{-3}), which are constructed from the soluble Nucleation, soluble Aitken and soluble accumulation mode modal parameters from the UKESM1 simulations when the criteria are fulfilled (criteria only uses soluble Aitken and soluble accumulation modes). The size distributions calculated using these UKESM1 modal parameters are in general less similar to the PNSD$_{NUM}$ than the monthly median SMEAR II size distributions are (Fig. 7c), because they

have more distinguished multimodal shapes, which arises from the modal representation of the PNSD. However, they still feature a minor accumulation mode in the presence of a large Aitken mode (with respect to N).

The UKESM1 results suggest that a strong spatiotemporal variability in the co-condensation driven ΔCDNC should be expected if this process were to be represented in GCMs. Consistently with the SMEAR II observations (Fig. 7a), spring months stand out as the times when the criteria are most likely to be met, but the other peak in the frequency, expected in September at SMEAR II, cannot be seen. Another interesting feature is the large spatial variability in the frequency. In March and April, a very evident hotspot can be seen in the southern parts of the boreal forest, more precisely in the north of Kazakhstan. When the whole northern hemisphere is displayed, it is clear that the hot spot region extends over Europe during Spring (Fig. S.13~~0~~) when the conditions favor the formation, growth and survival of small particles (Kerminen et al., 2018) as shown in Fig. S.14~~1~~ in terms of nucleation mode number concentration. The result therefore suggests high co-condensation potential in areas rich in ultrafine particles. The cloud response of co-condensation in an extended domain covering most of Eurasia could be an interesting follow-up study. However, such a study should incorporate also the condensation of nitric acid and ammonia, the concentrations of which are presumably abundant in the regions, where the co-condensation PNSD criteria are met (Kakavas et al., 2022). As this "Kazakhstan hotspot" is connected to aerosol phenomenology outside the boreal biome, the analysis is not continued further. Another evident springtime hot spot is located in North America, near the Rocky Mountains, but the updraft velocities at the area are not within the desired range ([0.2, 0.5] m s^{-1}) to yield significant cloud response from co-condensation (Fig. 7b).

Aside from these hotspots, it is notable that the overall background of the frequency of the times the criteria are met in the latitude range of [0, 75] °E increases from <2% to 2–6% when moving from March to April. This background stays elevated until June. Smaller hotspots within this area are visible and they correspond to regions known with high sulfur dioxide (SO_2) emissions, such as the Kola peninsula. The Kola peninsula SO_2 emissions have shown to trigger NPF events measured at SMEAR I in Finnish Eastern Lapland (e.g., Kyrö et al., 2014). An interesting next step would be to see how Fig. 7b changes with UKESM1 simulations incorporating boundary layer NPF and whether the percentage of times the criteria are met increases to values comparable with the SMEAR II observations and whether the frequency becomes larger also in Fall. Another interesting observation to be made from Fig. 7b is that no significant impact of co-condensation would be expected in UKESM1 in most of Siberia (East and Northeastern Siberia), which can be explained by the lack of nucleation mode particles in the UKESM1 simulations over the region (Fig. S.15~~2~~).

4 Conclusions

This study focuses on the role of the co-condensation of organic vapor and water on warm cloud microphysics in a boreal forest environment. Co-condensation has been proposed as a potentially significant process contributing to the feedbacks between VOC emissions, SOA loadings, cloud formation and climate. Boreal forests account for about a third of the Earth's forested area and are potentially significant sources of such co-condensing species.

First, PARSEC-UFO model is used to perform simulations for the BAECC measurement campaign which took place at the SMEAR II station in Southern Finland during 2014 (Petäjä et al., 2016). The measurement setup during BAECC was very advanced, enabling the initialization of PARSEC-UFO with state-of-the art data describing the ambient aerosol physical and chemical properties. The measurements conducted with the FIGAERO-I-CIMS (e.g., Mohr et al., 2017) are of high importance for this study due to the simultaneous

measurements of organic particle and vapor species. These data enable the incorporation of organic vapors from a broad volatility range into the PARSEC-UFO simulations. The previous modeling work on this topic used volatility distributions based on particle-phase measurements only, resulting in overall lower volatility and contributions of semi- and intermediate volatility organic vapor.

The results from the PARSEC-UFO simulations reveal that a competition effect exists between the reductions in maximum supersaturations and critical supersaturations needed for aerosol particle activation into cloud droplets when co-condensation is considered. The reductions in critical supersaturations are greater than the reductions in maximum supersaturation, which results in the simulated CDNC enhancements (simulations with co-condensation are compared against simulations without it under same meteorological conditions). The CDNC enhancements are of the order of 20% under realistic updraft velocities (0.1, 0.3, and 1 m s^{-1}) and correspond to reductions of 10–13 nm in the smallest activated dry diameters (~144 to ~128 nm, ~102 to ~88 nm, 72 to ~62 nm for the 0.1, 0.3, and 1 m s^{-1} updraft scenarios, respectively). The activation of smaller particles into cloud droplets results, as expected, in the formation of more numerous smaller cloud droplets. The critical supersaturation reductions result from the additions of soluble organic mass below cloud base along the simulated air parcels' adiabatic ascents while the reductions in maximum supersaturation are caused by the increasing condensation sink provided by more cloud droplets (the source of supersaturation is fixed as the meteorological conditions between simulations with and without co-condensation are kept constant).

The predicted CDNC enhancements are highest for the 0.3 m s^{-1} updraft velocities and depend on several, at least partly, interlinked parameters (see also Lowe et al., 2019). One parameter affecting the modelled CDNC is the availability of the co-condensable organic vapors, which in turn depends on the updraft velocities, the features of the organic volatility distribution as well as initial temperature and relative humidity. Most organic vapor condenses under the slowest adiabatic ascents and least in the highest due to kinetics. The organic volatility bins spanning from ELVOCs to the lower-volatility IVOCs condense in a similar, updraft-dependent, degree prior reaching the cloud base. Organic vapors of higher volatility involving species such as formic acid condense less efficiently and their condensation is sensitive to the presence of large particles, which are likely to activate regardless of co-condensation. Therefore, small enhancements in particularly SVOC and lower-volatility IVOC concentrations lead to significant enhancements in CDNC, while increases in the most volatile IVOCs and formic acid do not affect CDNC much.

The simulations performed with 0.3 m s^{-1} updrafts are repeated using volatility distributions from previous co-condensation studies (Cappa and Jimenez, 2010; Topping et al., 2013; Crooks et al., 2018). By doing so, the BAECC campaign median CDNC enhancement decreased from 22%~to non-significant values. This result is explained by the lower initialization temperature regulating organic vapor availability as well as lower SVOC and IVOC concentrations in previous studies, highlighting the added value of capturing these higher volatility bins within the VBS representations of atmospheric organic species. On the other hand, adding information on the LVOC and ELVOC range do not significantly influence the CDCN enhancements due to co-condensation.

The sensitivity of the modelled ΔCDNC to organic vapor concentrations is strongest when high maximum supersaturations (s_{max}>0.2% for the 0.3 m s^{-1} updraft scenarios) are reached. Such conditions are achieved when the dry PNSD surface area (a proxy for the condensation sink) remains below 100 μm^2 cm^{-3}. Under those conditions, CDNC enhancements exceeding 40% are predicted for conditions in which roughly 1 μg m^{-3} of co-condensable organic vapor is present.

Besides the meteorological conditions and the availability of co-condensable vapors, the CDNC enhancements depend critically on the size distribution of the initial aerosol population. Highest CDNC enhancements are generally achieved when the model is initialized with a relatively weak accumulation mode combined with a large nascent ultrafine particle mode with a geometric mean diameter of ca. 40 nm, with no visible Hoppel minimum present in the distribution. Such conditions are observed most frequently in Spring and September (about 30–40% of the time in years 2012–2017), when new particle formation events take place at SMEAR II.

Further on, UKESM1 simulations (years 2009–2013) are utilized to investigate the potential impact of including the process of co-condensation on droplet formation in this model over the whole boreal biome using the criteria developed from the SMEAR II case to identify most susceptible PNSD conditions. Overall, the UKESM1 PNSD are different from those observed at SMEAR II even when the strict criteria are used to select the ideal PNSD for co-condensation driven enhancements in CDNC. This discrepancy can arise from multiple causes such as the lack of critical aerosol processes (boundary layer new particle formation), but it could also be a common ESM feature arising from the modal representation of PNSD. Nonetheless, aside from two hotspots (one near the Rocky Mountains in North America, one over northern Kazakhstan, which are not analyzed further), the presence of suitable PNSD, as experienced by UKESM1, is most frequent over Fennoscandia and western parts of Siberia in spring, yet the frequencies at which those PNSD are modelled remained much lower than those obtained from the long-term SMEAR II PNSD measurements (2–6% in UKESM1). Perhaps surprisingly, suitable PNSD are never modeled over most of Siberia, suggesting that for the model configuration of UKESM1 used in this study, the process of co-condensation would not be expected to have an influence on droplet formation in this area. This is due to the low concentration of ultrafine particle particles modeled in the area.

In summary, these results highlight the potential significance of co-condensation in pristine boreal environments with a nascent ultrafine particle mode present. Such conditions are met over Fennoscandia and Western parts of Siberia in Spring and to a lesser extent in the Fall, when NPF takes place. For future modelling purposes, it is vital to stress the importance of the accurate representation of PNSD for capturing the role of co-condensation of organics on CDNC enhancements, including appropriate description of boundary layer NPF. Because the modelled CDNC enhancements are so significant, further research focus especially regarding observations of the co-condensation should be targeted in the future to motivate future assessments of co-condensation-driven radiative forcing. Perhaps this work inspires aircraft measurements (of the relevant parameters discussed in this paper) to take place over the Fennoscandia in the future to finally narrow down the importance of co-condensation for the accurate representation of CDNC in GCMs.

Appendix A

The effect of the initialization relative humidity, organic mass accommodation coefficient (α_{org}) and vaporization enthalpy (ΔH_{VAP}) on the modelled CDNC enhancements due to co-condensation are investigated for three individual simulationsdifferent conditions (simulation IDs #13, #55 and #95, respectively; Table S.1). The three simulations conditions were selected as they are representative of low, median and high ΔCDNC simulated during BAECC (simulation IDs #13, #55 and #95, respectively; Table S.1). Table A.1. describes the simulation setup for this sensitivity study.

Table A.1. The simulation setup for studying the sensitivities of initialization RH organic mass accommodation coefficient (α_{org}) and vaporization enthalpy (ΔH_{VAP}) on ΔCDNC is shown. Three simulation IDs are selected from the BAECC campaign (#13, #55 and #95, respectively; Table S.1) and three simulation sets (for varying initialization RH, α_{org} and ΔH_{VAP}, respectively) are performed for each ID with and without co-condensation. The initial temperature, aerosol chemical composition and PNSD vary between the different IDs, and are taken from Table S.1. A fixed updraft velocity of 0.3 m s⁻¹ is applied for all the different simulations.

Set	Co-condensation	Initialization RH [%]	α_{org}	ΔH_{VAP} [kJ mol⁻¹]
1a	OFF	[60, 80, 90, 95, 99]	1	150
1b	ON	[60, 80, 90, 95, 99]	1	150
2a	OFF	90	[0, 0.2, 0.4, 0.6, 0.8. 1.0]	150
2b	ON	90	[0, 0.2, 0.4, 0.6, 0.8. 1.0]	150
3a	OFF	90	1	[80, 100, 120, 150, 200]
3b	ON	90	1	[80, 100, 120, 150, 200]

The initialization RH affects the availability of organic vapor for co-condensation: when PARSEC-UFO is initialized under high RH (~>95%), most organic vapor is scavenged at initial conditions causing negligible enhancements in CDNC. On the other hand, if the initialization RH is lower (<90%), less organic vapor is scavenged at initial conditions, and the modeled ΔCDNC are greater (Fig. A.1). By varying α_{org}, the effect of the assumption of ideality has on the projected CDNC enhancements is probed. For simplicity, the mass accommodation coefficient for organics (α_{org}) is set to be constant across the volatility bins. By reducing α_{org} from 1 to 0.8, the condensation of organics reduces. However, this impacts CDNC only in the simulation ID #95 (Fig. A.2; CDNC reduces from ~62% to 55%), i.e., simulation with the highest ΔCDNC. When α_{org} < 0.4, also the simulation ID #55 shows a reduction in the modeled ΔCDNC as it drops from ~22% to ~15%. The selection of the enthalpy of vaporization for organics does not affect ΔCDNC (Fig. A.3). Over all, the initial relative humidity plays the most critical role out of the three parameters considered here (RH, α_{org} and ΔH_{VAP}), on the modelled ΔCDNC.
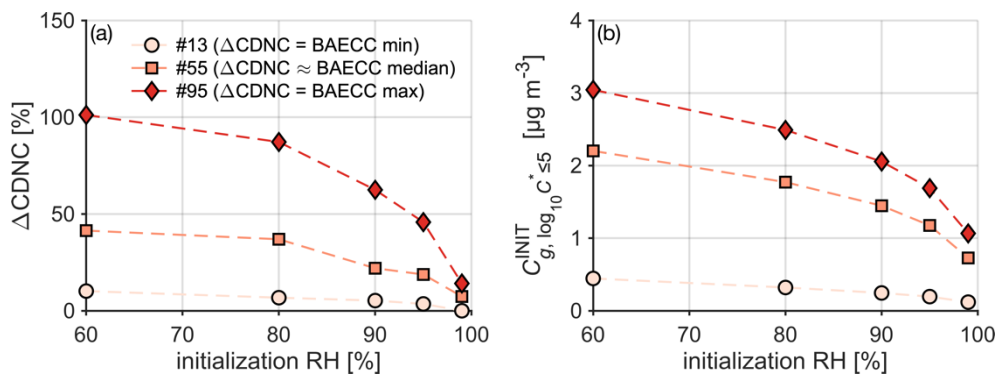
Figure A.1 The modelled CDNC enhancements as function of initialization RH ranging from 60% to 99% (indicated with different colors) for each simulation ID are shown, respectively. The initialization temperature and pressure are fixed to values shown in Table S.1. and only the volatility bins $\log_{10}C^* \leq 5$ are included, which is motivated e.g., by Fig. 4. The simulations are performed with an updraft velocity of 0.3 m s⁻¹. The markers with

988 the lightest color refer to the BAECC simulation, where co-condensation influenced ΔCDNC negligibly (ID #13,
989 ΔCDNC = 3%), the orange markers to the BAECC median ΔCDNC (ID #55), and the red markers represent a
990 simulation, where the modelled ΔCDNC was greatest (ID #95, ΔCDNC = 75%). ΔCDNC is calculated 50 m above
991 CB based on critical radii, similarly to the study.
992
993
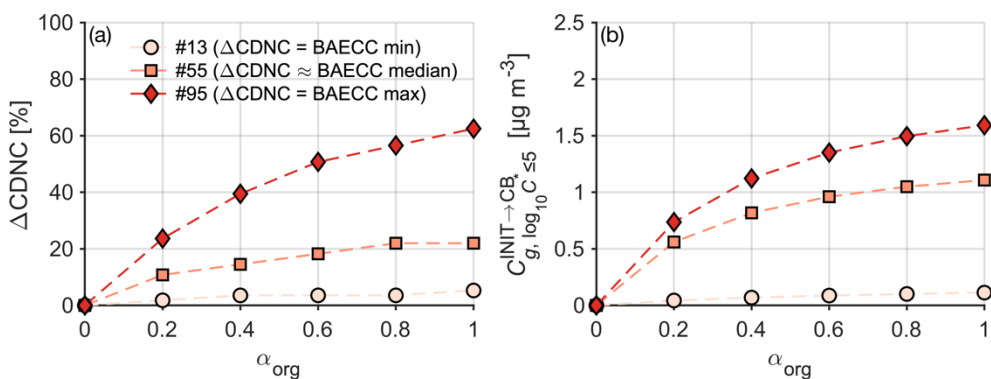
994
995 **Figure A.2** The modelled CDNC enhancements as function of mass accommodation coefficient for organics (α_{org})
996 ranging from zero to one. The colorings and presented simulations are same as in Fig. A.1.
997
998
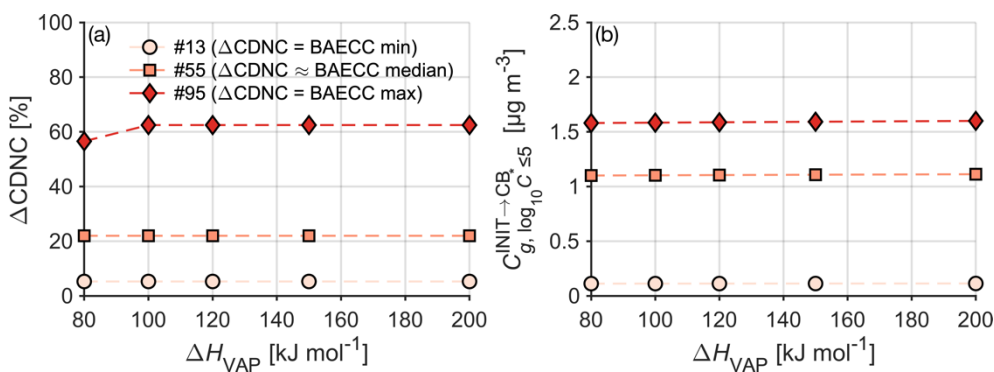
999
1000
1001 **Figure A.3** The modelled CDNC enhancements as function of vaporization enthalpy for organics (ΔH_{VAP}) ranging
1002 from zero to one. The colorings and presented simulations are same as in Fig. A.1.
1003

1004

Data availability

1006 The PARSEC-UFO input and outputs for reproducing the figures will be available on the Bolin Centre database.

1007

Competing interests

1009 The authors have the following competing interests: Some authors are members of the editorial board of
1010 Atmospheric Chemistry and Physics. The peer-review process will be guided by an independent editor. One or
1011 more authors have received funding from European Union's Horizon 2020 research and innovation programme,
1012 European Research Council, Knut and Alice Wallenberg foundation, Academy of Finland and US Department of
1013 Energy, UK Natural Environment Research Council (NERC), and/or support from ACTRIS Translational Access
1014 and ACTRIS-HY. The authors have no other competing interests to declare.

Author contributions

1016 LH, IR, DGP and CM conceptualized the idea of the study and designed the simulations. LH prepared the
1017 PARSEC-UFO input data, performed the PARSEC-UFO simulations, analyzed the simulation outputs, made the
1018 majority of the figures and wrote the manuscript with contributions from the coauthors. TP designed and led the
1019 BAECC campaign. CM performed the FIGAERO-I-CIMS measurements, WH processed and delivered the
1020 FIGAERO-I-CIMS data and gave input on the volatility distribution calculation. RR assisted LH with the
1021 radiosonde data, provided the hygroscopicity seasonal cycle data and contributed to the PARSEC-UFO
1022 description writing. ET and DGP performed the UKESM1 simulations and DGP designed and processed the data
1023 for analysis input parameters to droplet activation parameterization. DGP and PB created PARSEC and extended
1024 it to include UFO, provided documentation for PARSEC-UFO and contribution to description. SB visualized the
1025 UKESM1 data, assisted LH with FORTRAN programming and gave input on the data interpretation.

Acknowledgements

1027 We gratefully acknowledge Samuel Lowe for developing the unified framework for organics onto the ICPM
1028 (Lowe, 2020), the useful discussions, code and support. We acknowledge Ellie Duncan for useful discussions and
1029 support regarding the UKESM1 data and Megan Haslum for their documentation on PARSEC-UFO Köhler terms.
1030 We acknowledge Pasi Aalto and SMEAR II staff for their efforts during the BAECC campaign. We thank Dmitri
1031 Moisseev, Federico Bianchi and Annica Ekman for useful discussions. We acknowledge the Atmospheric
1032 Radiation Measurement (ARM) Program for their inputs during BAECC, the interpolated radiosonde data were
1033 obtained from the ARM Program sponsored by the U.S. Department of Energy, Office of Science, Office of
1034 Biological and Environmental Research, Climate and Environmental Sciences Division. We acknowledge use of
1035 the Monsoon2 system, a collaborative facility supplied under the Joint Weather and Climate Research Programme,
1036 a strategic partnership between the Met Office and the Natural Environment Research Council. We also thank all
1037 the people responsible for the development of UKESM1. DGP would like to extend a personal thanks to Dr
1038 Alistair Sellar, who provided support for the configuration of the UKESM1 simulations performed as part of the
1039 AeroCom GCM Trajectory experiment on which these simulations are based.

Funding

1041 Financial support from the European Union's Horizon 2020 research and innovation programme (project FORCeS
1042 under grant agreement No 821205, project FOCI under grant agreement No101056783, project CRiceS under
1043 grant agreement No 101003826), European Research Council (Consolidator grant INTEGRATE No 865799,
1044 starting grant CHAPAs No 850614), and Knut and Alice Wallenberg foundation (Wallenberg Academy
1045 Fellowship projects AtmoRemove No 2015.0162 and CLOUDFORM No 2017.0165) , Academy of Finland via a
1046 Flagship programme for Atmospheric and Climate Competence Center (ACCC, No 337549) and projects No
1047 353386, 334792, 340791, 325681 are gratefully acknowledged. The BAECC campaign was supported by US
1048 Department of Energy (Petäjä, No DE-SC0010711) and additional measurements were supported via ACTRIS
1049 Transnational Access. University of Helsinki is acknowledged for supporting the SMEAR II station via ACTRIS-
1050 HY. DGP and PB acknowledge support from Natural Environment Research Council (NERC) grant no.
1051 NE/W001713/1 for the creation of the Pseudo-Adiabatic bin-micRophySics university of Exeter Cloud parcel
1052 model (PARSEC) and for adding Unified Framework for Organics (UFO) to PARSEC to create PARSEC-UFO.
1053 ET acknowledges support from NERC GW4+ grant no. NE/L002434/1 and DGP from NERC grant no.

NE/W001713/1 for developments to the UKESM1 activation scheme and configuration of the UKSEM1 simulations.

Tables

1059 **Table 1** Overview of the PARSEC-UFO simulation input parameters that remain unchanged in all of the
1060 simulation sets conducted with or without co-condensation. The updraft velocities, organic volatility distributions
1061 and organic vapor concentrations that change between simulation sets are reported in Table 2 together with the
1062 median model outputs. The time series of these model input data are shown in Fig.1. All the modelling scenarios
1063 are initiated at 90% relative humidity.

Parameter	Min	Max	Median
Aitken mode number conc. N_1 [cm^{-3}] [a]	160	12 316	1491
Accumulation mode number conc. N_2 [cm^{-3}] [a]	44	2 433	560
Aitken mode geometric mean dry diameter D_1 [nm] [a]	7.1	71.0	23.8
Accumulation mode geometric mean dry diameter D_2 [nm] [a]	62.6	201.9	115.3
Geom. standard deviation of Aitken mode σ_1 [a]	1.50	2.08	1.75
Geom. standard deviation of accumulation mode σ_2 [a]	1.33	2.06	1.75
Number of PNSD size bins	400	400	400
Organic mass fraction f_{Org} [%] [b]	25	84	68
Ammonium sulfate mass fraction f_{AS} [%] [c]	12	75	32
Initial T [K] [de]	271	295	279
Initial p [hPa]	980	980	980
Initial RH [%]	90	90	90
Mass accommodation coefficient α	1	1	1
Vaporization enthalpy for organics ΔH_{vap} [kJ mol^{-1}] [ed]	150	150	150
Effective soluble fraction of organics	1	1	1
Surface tension γ [mN m^{-1}]	72.8	72.8	72.8

1064 [a] Retrieved from fits assigned onto the measured aerosol size distributions (Aalto et al., 2001) using a fitting algorithm by Hussein et al.
1065 (2005).
1066 [b] Retrieved from aerosol chemical composition measurements (Heikkinen et al., 2020).
1067 [c] $f_{AS} = 1- f_{Org}$
1068 [de] Retrieved from radio soundings (ARM Data Center, 2014). The temperatures shown were recorded when the relative humidity measured
1069 by the radiosonde reached 90%, i.e., the initial relative humidity used for the adiabatic ascents.
1070 [ed] Note that in the volatility distribution construction (offline from PARSEC) the ΔH_{vap} is temperature-adjusted following Epstein et al. (2010).
1071

Table 3 Overview of the PARSEC-UFO simulation output for the no co-condensation (noCC) and co-condensation (CC with F volatility distribution) simulations performed using varying updraft velocities.

Parameter	Median		
Updraft velocity w [m s^{-1}] [a]	0.1	0.3	1.0
Parcel displacement before CB [m]	190	190	190
Cloud droplet number conc. $\text{CDNC}_{\text{noCC}}$ [cm^{-3}] [b]	158	292	523
Cloud droplet number conc. CDNC_{CC} [cm^{-3}] [b]	186	400	618
CDNC enhancement ΔCDNC [%] [b]	15.6	22.1	18.9
Maximum supersaturation $s_{\max}^{\text{noCC}}$ [%]	0.14	0.24	0.40
Maximum supersaturation $s_{\max}^{\text{CC}}$ [%]	0.14	0.22	0.38
Smallest activated dry radius r_{noCC}^{*} [nm]	72	51	36
Smallest activated dry radius r_{CC}^{*} [nm]	64	44	31
Initial organic vapor conc. $\sum C_g^{\text{INIT}}$ [µg m^{-3}]	22.05	2.05	2.05
Organic vapor condensed below cloud base $\sum C_g^{\text{INIT}} - \sum C_g^{\text{CB}}$ [µg m^{-3}]	1.82	1.41	0.55
Fraction of organic vapor condensed below cloud base $\Delta C_g^{\text{INIT}\rightarrow\text{CB}}$ [%]	91	70	28

[a] Model input parameters crucial for understanding the differences between the co-condensation simulation model outputs.
[b] The CDNC represent the integrated number concentration in size bins exceeding the critical radius in wet size at 50 meters above cloud base (CB).
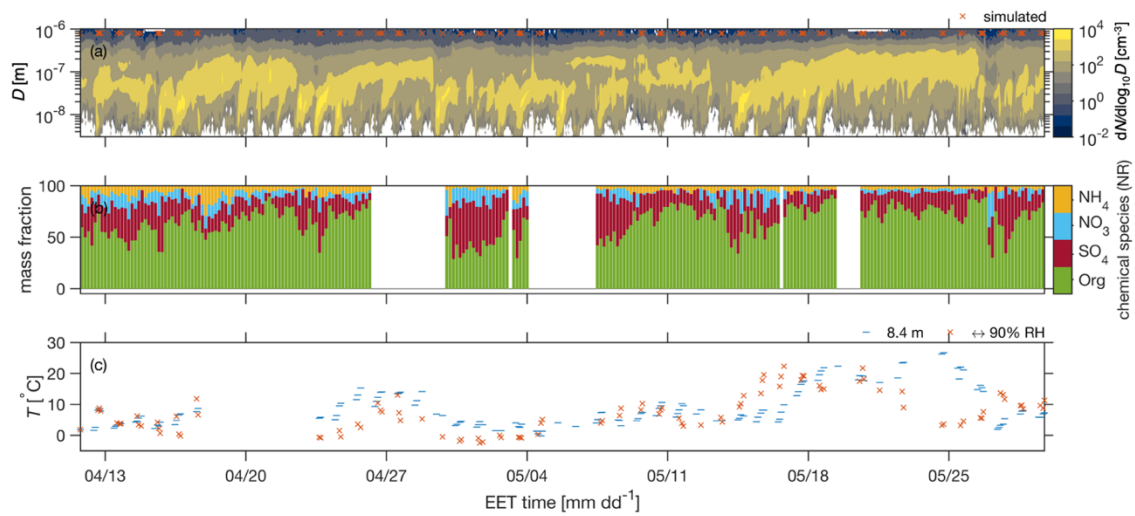
Figures

Figure 1 (**a**) Time-series of the particle number size distribution in the time period of interest during BAECC. The time points used for the PARSEC-UFO initialization are shown as red/orange crosses. (**b**) The non-refractory (NR) chemical composition of sub-micrometer aerosol particles for the same time period. (**c**) The time series of ambient temperature near ground level (8.4 m a.g.l.) is shown in blue and the PARSEC-UFO initialization temperature corresponding to RH = 90% from the interpolated radiosonde data product is shown in orange. The subpanels have a common x–axis representing the East European winter time (UTC+2).
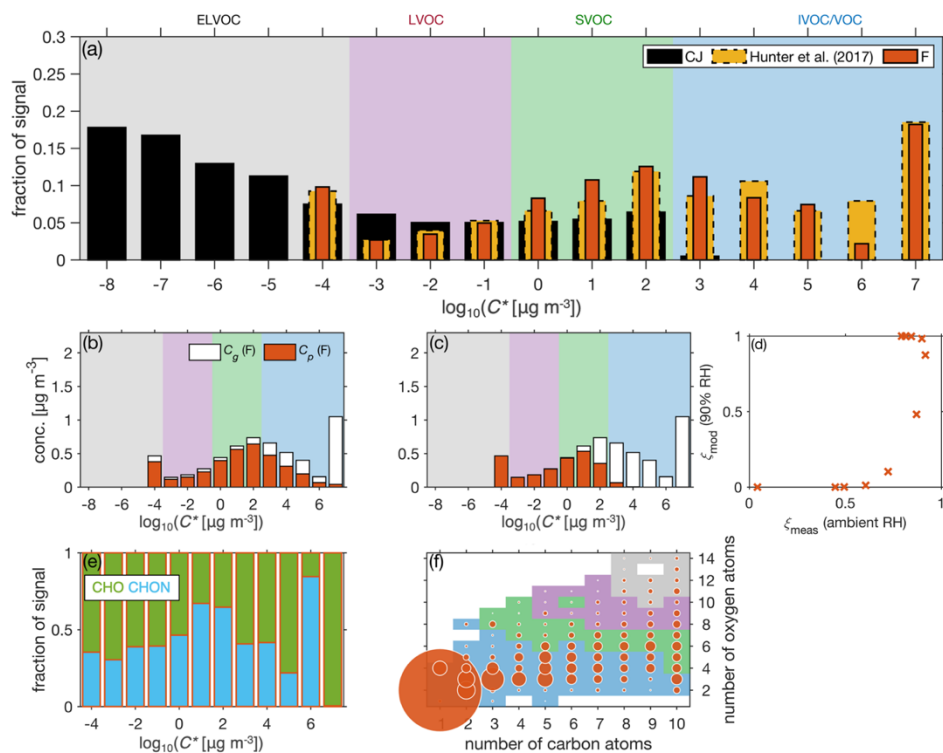
Figure 2 (a) The normalized volatility distributions ($C_g + C_p$) from Cappa and Jimenez (2010; CJ) and the BAECC FIGAERO-I-CIMS measurements (F) using the modified Li et al. (2016) molecular formulae-based parameterizations. A volatility distribution from Hunter et al. (2017) constructed from the BEACHON-RoMBAS measurement campaign is shown by the dashed bars. The volatility ranges for ELVOC, LVOC, SVOC and IVOC/VOC are shown in color scales. These C^* limits apply throughout the paper. (**b–c**) The partitioning predicted based on the FIGAERO-I-CIMS gas- and particle-phase measurements and the PARSEC-UFO, respectively. The PARSEC-UFO partitioning corresponds to 90% RH while the ambient observation is under ambient RH. (**d**) A scatterplot drawn between the FIGAERO-I-CIMS derived partitioning coefficients (ξ_{meas}) and PARSEC-UFO-derived coefficients (ξ_{mod}) for the 12 different volatility bins. Panels (**e–f**) represent the gas phase molecular composition from the FIGAERO-I-CIMS: panel (**e**) the distribution between organic nitrates and non-nitrates and panel (**f**) the degree of oxygenation in the form of oxygen and carbon numbers. The marker size in panel **f** corresponds to the concentration of signal for the given n_C and n_O combination.
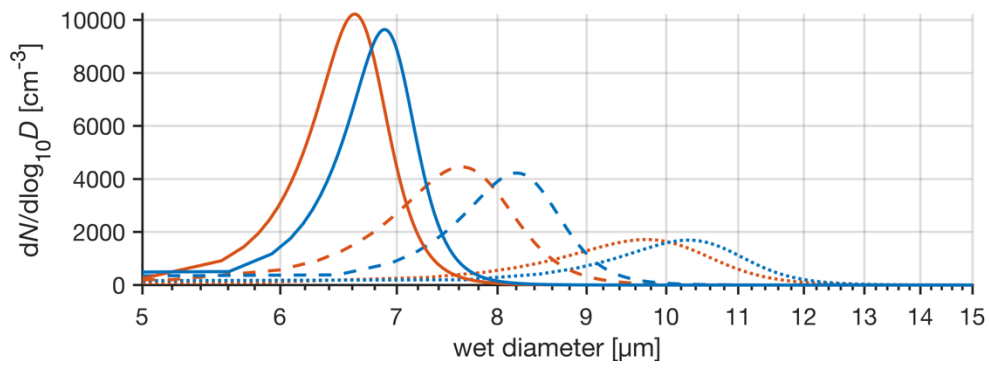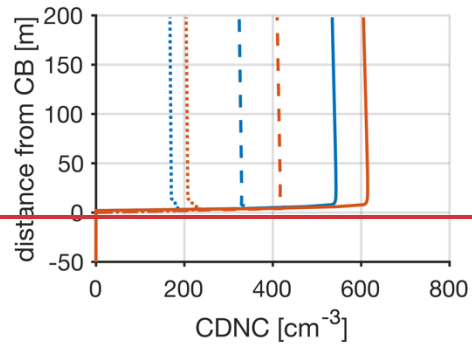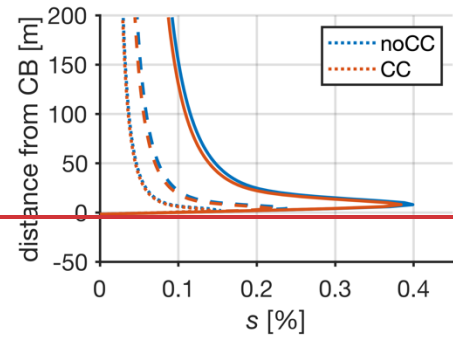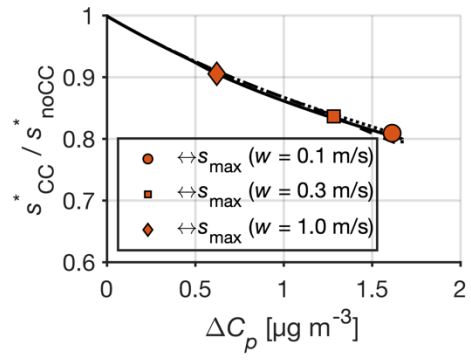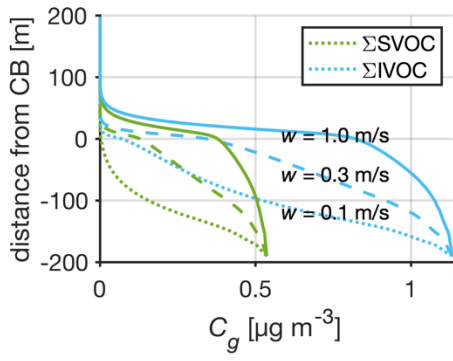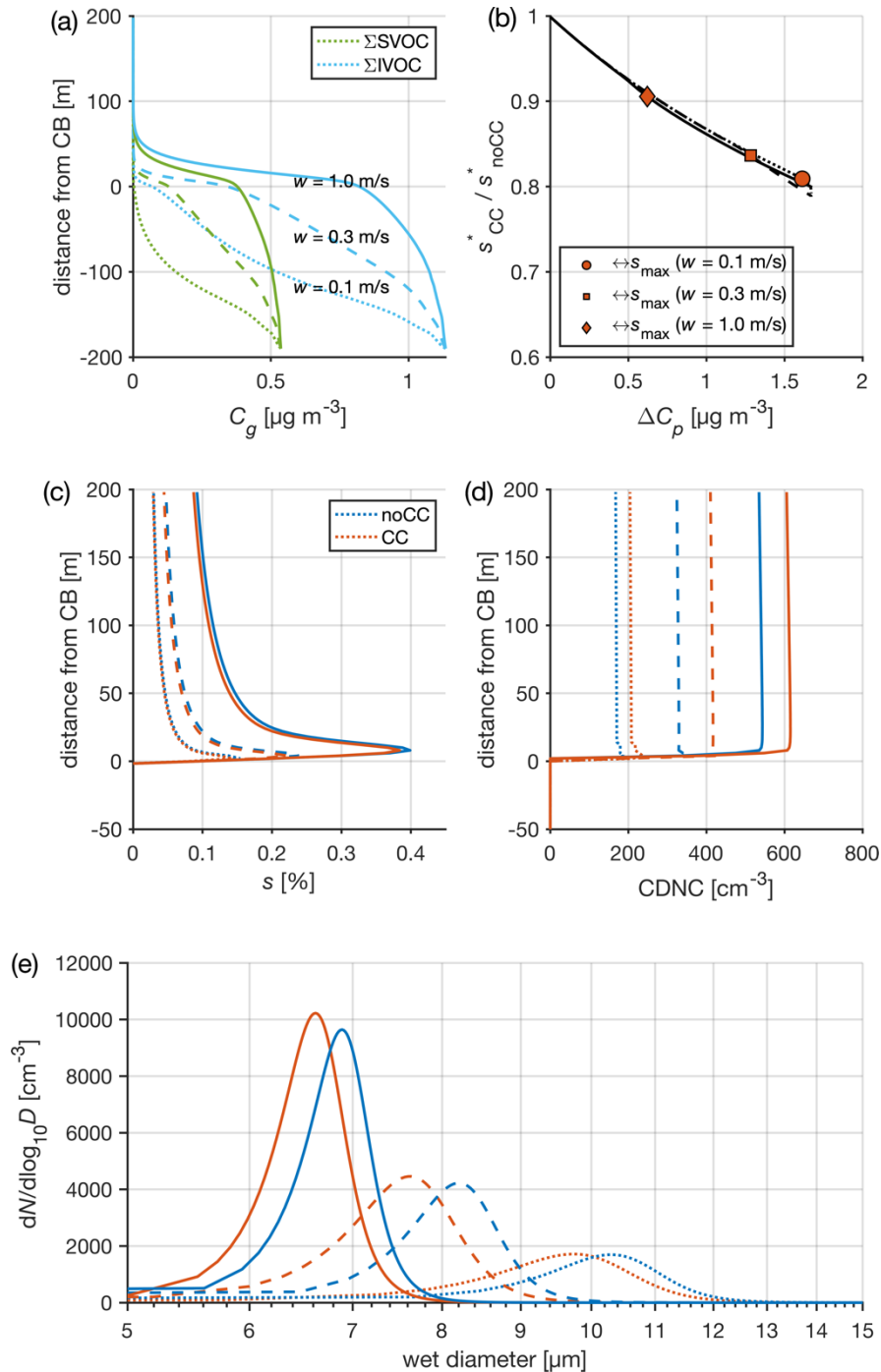
Figure 3 A summary of simulated cloud microphysics on May 11, 13:37 EET during the BAECC campaign. Simulations are performed both with and without organic condensation (red and blue lines, respectively) for three different updraft velocities (see line styles from panel **a**). The initial temperature is 279 K, pressure 980 hPa and ~~supersaturation 0.1% (~~RH =~~is~~ 90%~~)~~. (**a**) The concentration of SVOCs and IVOCs in the gas phase as a function of distance from cloud base (CB). SVOCs have $\log_{10}C^* = [0, 2]$ and IVOCs $\log_{10}C^* = [3, 7]$ under 279 K. (**b**) The relative change in critical supersaturation (s^*) between noCC and CC simulations, as a function of soluble mass added along the ascent by condensing organics in the simulations, where co-condensation is enabled. The data are shown for a particle with a dry diameter of 147 nm at PARSEC-UFO initialization. The markers represent the reductions at the time when maximum supersaturation (s_{max}) was reached. ~~The absolute change in critical supersaturation as a function of soluble mass added along the ascent by condensing organics. The markers represent the reductions at the maximum supersaturation (s_{max}).~~ (**c–d**) The evolution of the s_{max} and CDNC with altitude, respectively. (**e**) The droplet spectra 50 meters above CB. Size bins exceeding the critical diameter as predicted by Köhler theory are calculated as cloud droplets. The red lines are obtained with F volatility distributions (**Fig. 2a**). The line type specifications in panels **d–e** follow those shown in panel **a** and the colors used in panels **d–e** are documented in the panel **c** legend.
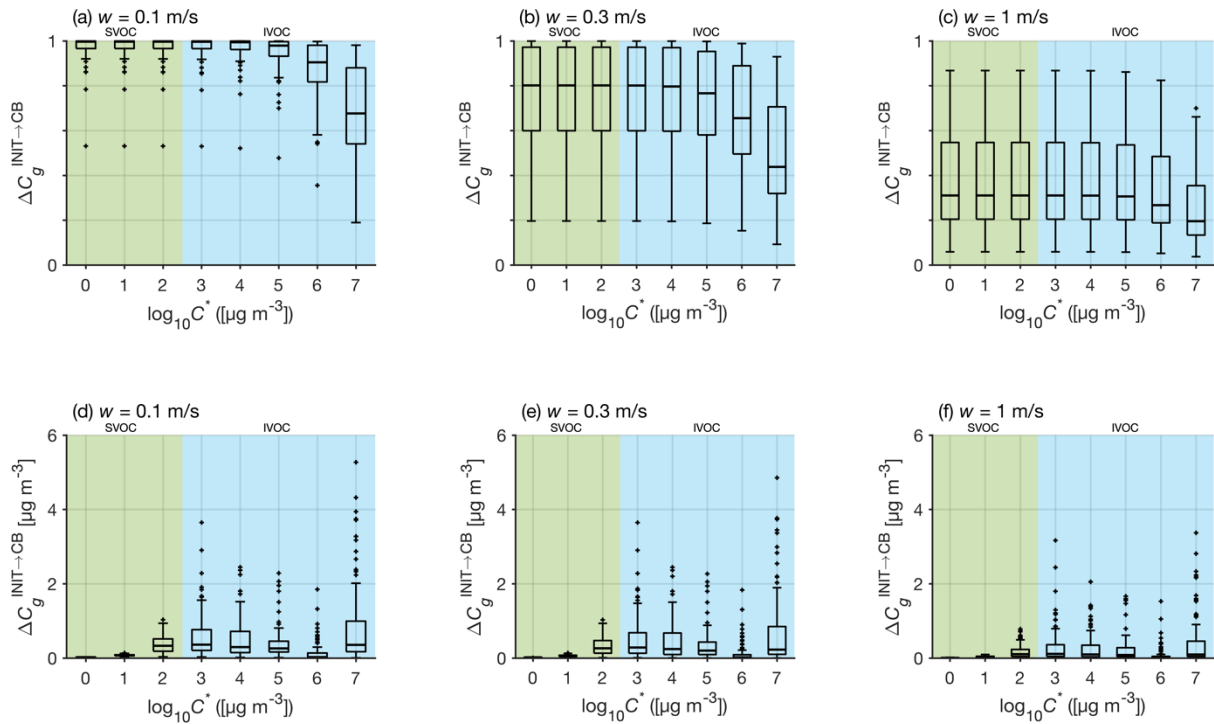
Figure 4 Box plots showing the fractions (**a–c**) and absolute concentrations (**d–f**) of organic vapor condensed below cloud base per volatility bin for the 0.1, 0.3 and 1.0 m s^{-1} updraft scenarios, respectively. The shaded backgrounds reflect SVOC (green) and IVOC/VOC (blue) volatility ranges under PARSEC-UFO initialization temperature.
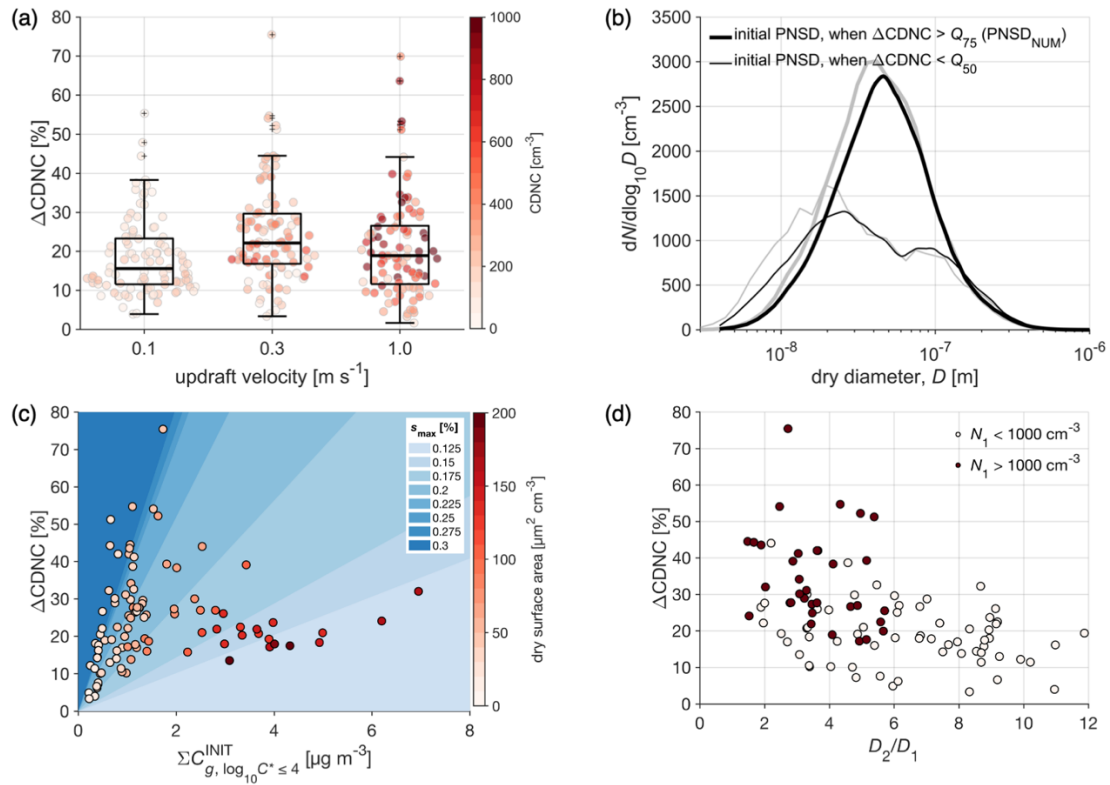
1129
1130
1131 **Figure 5 (a)** Box plots showing the predicted ΔCDNC (using F volatility distributions) due to co-condensation in the three
1132 different modelling scenarios (0.1, 0.3 and 1.0 m s^{-1} updrafts). The colorful markers represent CDNC (without accounting for
1133 co-condensation) in form of a swarmplot. The median (Q_{50}) ΔCDNC yielded using the CJ distribution are shown in Fig. S.7.
1134 **(b)** The median initial dry size distributions calculated from the simulations exceeding the 75th percentile in ΔCDNC ($>Q_{75}$;
1135 thick lines) and remaining below the ΔCDNC median ($<Q_{50}$; thin lines), respectively. The PNSD medians are calculated by
1136 taking a median of the PNSD calculated using the log-normal parameters from both sets of simulations (in black) and from
1137 the measurement data (in grey). The data are shown for the simulation performed with a 0.3 m s^{-1} updraft. **(c)** The relationship
1138 between the modeled ΔCDNC and the initial organic vapor concentration within the $\log_{10}C^*$ range from -4 to 4 ($C_{g,\,-4:4}^{INIT}$). The
1139 marker color-coding represents the initial dry size distribution surface area (S). The plot background is colored with the
1140 modeled maximum supersaturations (s_{max}). These are calculated from s_{max} binned ΔCDNC vs $C_{g,\,-4:4}^{INIT}$ linear fit 90% confidence
1141 intervals (CI; area between CI is colored). The figure shows that S anticorrelates with s_{max} (see Eq. 3). The data are shown for
1142 the simulations performed with a 0.3 m s^{-1} updraft only. **(d)** The figure evaluates how well the simple criteria ($D_2/D_1<6$ and
1143 $N_1>1000$ cm^{-3}) works on the PARSEC-UFO simulations.
1144
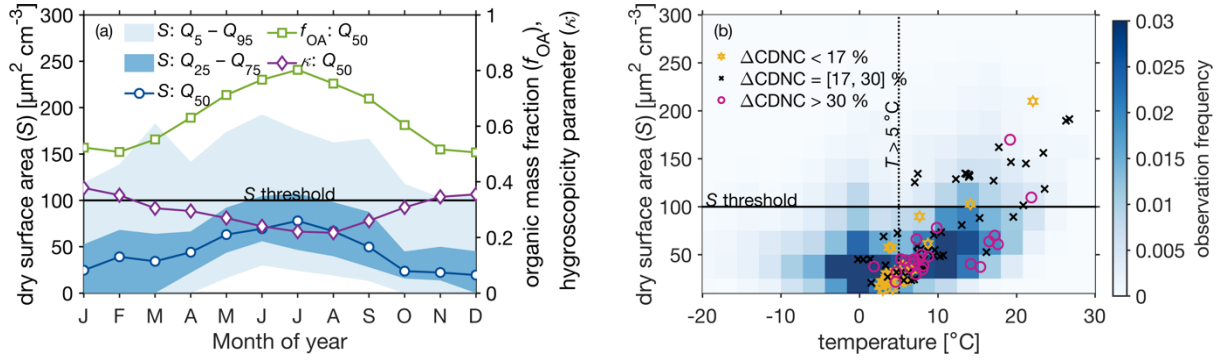
Figure 6 (a) The seasonal cycle of the dry aerosol size distribution surface area (S) calculated from the long-term aerosol size distribution observations (2012–2017; left y-axis), where the markers represent the median values, the darkest shading the interquartile range and the lighter shading the area between the 5th and 95th percentiles. The panel also contains the median seasonal cycles of organic mass fraction and the κ hygroscopicity parameter compiled from the same long-term period (right y-axis). The green horizontal line refers to the dry surface area threshold of 100 μm^2 cm^{-3} from Fig. 5, under which the greatest $\Delta CDNC$ are modeled using the BAECC data. **(b)** A density plot showing the observations of S under different ambient temperatures during the 2012–2017 long-term period. The S threshold of 100 μm^2 cm^{-3} is again shown with the horizontal green line. The vertical dashed green line is a rough estimate for the start of the thermal growing season, which also refers to the starting point of the majority of the BVOC emissions. The markers show the PARSEC-UFO simulation data color-coded with the associated $\Delta CDNC$ (simulations yielding the $\Delta CDNC$ below the 25th percentile are shown in blue, simulations yielding $\Delta CDNC$ above the 75th percentile in red and the simulations between those limits are shown in white).
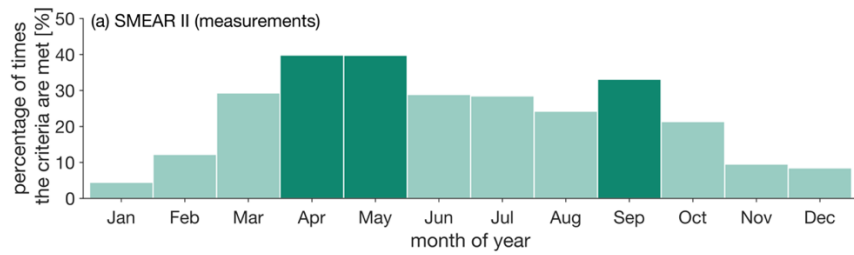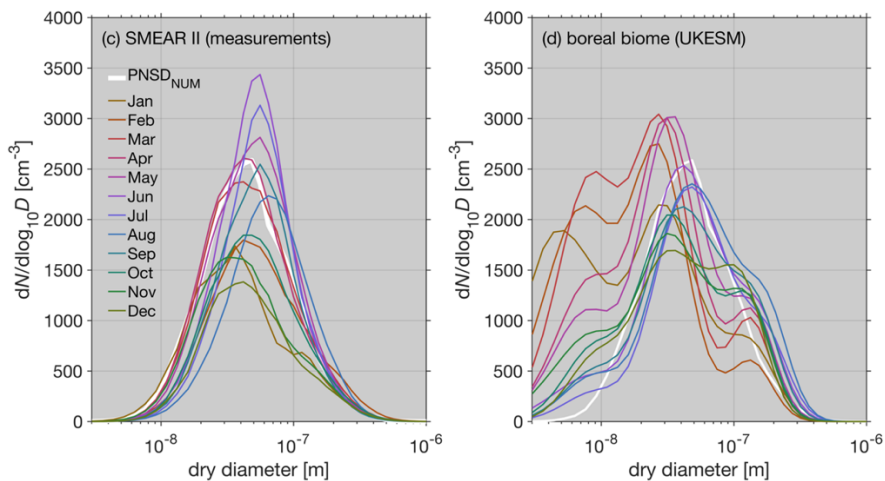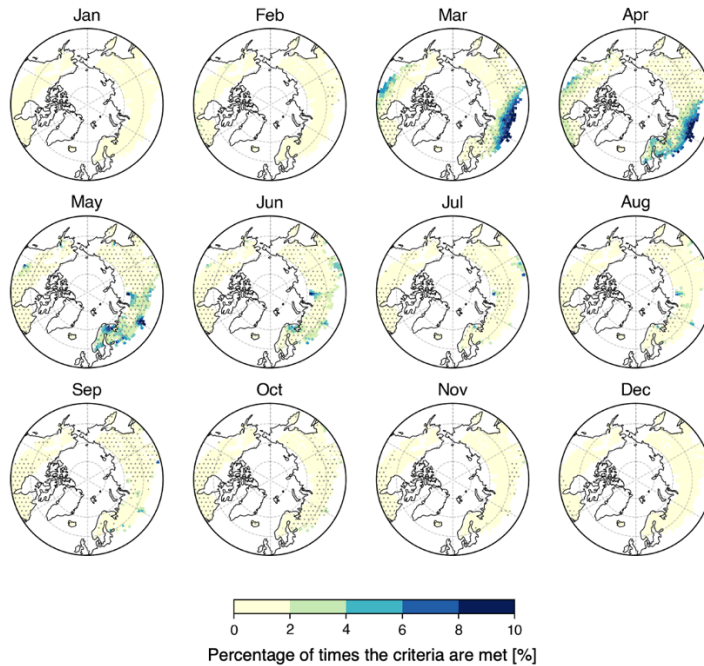
Figure 7 (a) Percentage of times the criteria ($D_2/D_1<6$ and $N_1>1000$ cm^{-3}) are met at SMEAR II between the 2012–2017 measurement period. D_2, D_1 and N_1 are attained from bimodal fits calculated for the measured PNSD using the Hussein et al. (2005) algorithm. **(b)** The percentage of times the criteria are met in a 2009–2013 UKESM1 simulation. D_2, D_1 and N_1 are the ~~log-normal~~ ~~modal~~ parameters representing the soluble accumulation mode and soluble Aitken mode~~s~~ ~~parameters~~. The gray markers refer to boreal grid cells, where the median updraft velocity at cloud base is between 0.2 and 0.5 m s^{-1}. **(c–d)** Monthly median size distributions from the long-term PNSD measurements at SMEAR II and UKESM1 simulation, respectively. The UKESM1 size distributions are calculated from the log-normal PNSD parameters for nucleation, soluble Aitken and soluble accumulation modes assuming geometric standard deviations of $\sigma = 1.59$ for nucleation and soluble Aitken modes and $\sigma = 1.4$ for the soluble accumulation mode. The soluble coarse mode is not included in the analysis.

References

1172 Aalto, P., Hämeri, K., Becker, E., Weber, R., Salm, J., Mäkelä, J. M., Hoell, C., O'dowd, C. D., Hansson, H.-C., Väkevä, M., Koponen, I. K., Buzorius, G., and Kulmala, M.: Physical characterization of aerosol particles during nucleation events, Tellus B: Chemical and Physical Meteorology, 53, 344–358, https://doi.org/10.3402/tellusb.v53i4.17127, 2001.

Abdul-Razzak, H. and Ghan, S. J.: A parameterization of aerosol activation: 2. Multiple aerosol types, Journal of Geophysical Research: Atmospheres, 105, 6837–6844, https://doi.org/10.1029/1999JD901161, 2000.

Äijälä, M., Heikkinen, L., Fröhlich, R., Canonaco, F., Prévôt, A. S. H., Junninen, H., Petäjä, T., Kulmala, M., Worsnop, D., and Ehn, M.: Resolving anthropogenic aerosol pollution types – deconvolution and exploratory classification of pollution events, Atmospheric Chemistry and Physics, 17, 3165–3197, https://doi.org/10.5194/acp-17-3165-2017, 2017.

Allan, J. D., Alfarra, M. R., Bower, K. N., Coe, H., Jayne, J. T., Worsnop, D. R., Aalto, P. P., Kulmala, M., Hyötyläinen, T., Cavalli, F., and Laaksonen, A.: Size and composition measurements of background aerosol and new particle growth in a Finnish forest during QUEST 2 using an Aerodyne Aerosol Mass Spectrometer, Atmos. Chem. Phys., 6, 315–327, https://doi.org/10.5194/acp-6-315-2006, 2006.

AeroCom: https://aerocom.met.no/, last access: 21 November 2022.

ARM Data Center: Atmospheric Radiation Measurement (ARM) user facility. 2014, updated hourly. Interpolated Sonde (INTERPOLATEDSONDE). 2014-04-01 to 2014-07-01, ARM Mobile Facility (TMP) U. of Helsinki Research Station (SMEAR II), Hyytiala, Finland; AMF2 (M1). Compiled by M. Jensen, S. Giangrande, T. Fairless and A. Zhou., 2014.

Artaxo, P., Hansson, H.-C., Andreae, M. O., Bäck, J., Alves, E. G., Barbosa, H. M. J., Bender, F., Bourtsoukidis, E., Carbone, S., Chi, J., Decesari, S., Després, V. R., Ditas, F., Ezhova, E., Fuzzi, S., Hasselquist, N. J., Heintzenberg, J., Holanda, B. A., Guenther, A., Hakola, H., Heikkinen, L., Kerminen, V.-M., Kontkanen, J., Krejci, R., Kulmala, M., Lavric, J. V., Leeuw, G. de, Lehtipalo, K., Machado, L. A. T., McFiggans, G., Franco, M. A. M., Meller, B. B., Morais, F. G., Mohr, C., Morgan, W., Nilsson, M. B., Peichl, M., Petäjä, T., Praß, M., Pöhlker, C., Pöhlker, M. L., Pöschl, U., Randow, C. V., Riipinen, I., Rinne, J., Rizzo, L. V., Rosenfeld, D., Dias, M. A. F. S., Sogacheva, L., Stier, P., Swietlicki, E., Sörgel, M., Tunved, P., Virkkula, A., Wang, J., Weber, B., Yáñez-Serrano, A. M., Zieger, P., Mikhailov, E., Smith, J. N., and Kesselmeier, J.: Tropical and Boreal Forest – Atmosphere Interactions: A Review, Tellus B: Chemical and Physical Meteorology, 74, 24–163, https://doi.org/10.16993/tellusb.34, 2022.

Barahona, D., West, R. E. L., Stier, P., Romakkaniemi, S., Kokkola, H., and Nenes, A.: Comprehensively accounting for the effect of giant CCN in cloud activation parameterizations, Atmospheric Chemistry and Physics, 10, 2467–2473, https://doi.org/10.5194/acp-10-2467-2010, 2010.

Bardakov, R., Riipinen, I., Krejci, R., Savre, J., Thornton, J. A., and Ekman, A. M. L.: A Novel Framework to Study Trace Gas Transport in Deep Convective Clouds, Journal of Advances in Modeling Earth Systems, 12, e2019MS001931, https://doi.org/10.1029/2019MS001931, 2020.

Barley, M., Topping, D. O., Jenkin, M. E., and McFiggans, G.: Sensitivities of the absorptive partitioning model of secondary organic aerosol formation to the inclusion of water, Atmos. Chem. Phys., 9, 2919–2932, https://doi.org/10.5194/acp-9-2919-2009, 2009.

Bellouin, N., Quaas, J., Gryspeerdt, E., Kinne, S., Stier, P., Watson-Parris, D., Boucher, O., Carslaw, K. S., Christensen, M., Daniau, A.-L., Dufresne, J.-L., Feingold, G., Fiedler, S., Forster, P., Gettelman, A., Haywood, J. M., Lohmann, U., Malavelle, F., Mauritsen, T., McCoy, D. T., Myhre, G., Mülmenstädt, J., Neubauer, D., Possner, A., Rugenstein, M., Sato, Y., Schulz, M., Schwartz, S. E., Sourdeval, O., Storelvmo, T., Toll, V., Winker, D., and Stevens, B.: Bounding Global Aerosol

Radiative Forcing of Climate Change, Reviews of Geophysics, 58, e2019RG000660, https://doi.org/10.1029/2019RG000660, 2020.

Boucher, O., Randall, D., Artaxo, P., Bretherton, C., Feingold, G., Forster, P., Kerminen, V.-M., Kondo, Y., Liao, H., Lohmann, U., Rasch, P., Satheesh, S. K., Sherwood, S., Stevens, B., Zhang, X. Y., Stocker, T. F., Qin, D., Plattner, G.-K., Tignor, M., Allen, S. K., Boschung, J., Nauels, A., Xia, Y., Bex, V., and Midgley, P. M.: Clouds and Aerosols. In: Climate Change 2013: The Physical Science Basis. Contribution of Working Group I to the Fifth Assessment Report of the Intergovernmental Panel on Climate Change, Cambridge University Press, 2013.

Canagaratna, M. r., Jayne, J. t., Jimenez, J. l., Allan, J. d., Alfarra, M. r., Zhang, Q., Onasch, T. b., Drewnick, F., Coe, H., Middlebrook, A., Delia, A., Williams, L. r., Trimborn, A. m., Northway, M. j., DeCarlo, P. f., Kolb, C. e., Davidovits, P., and Worsnop, D. r.: Chemical and microphysical characterization of ambient aerosols with the aerodyne aerosol mass spectrometer, Mass Spectrometry Reviews, 26, 185–222, https://doi.org/10.1002/mas.20115, 2007.

Cappa, C. D.: A model of aerosol evaporation kinetics in a thermodenuder, Atmos. Meas. Tech., 3, 579–592, https://doi.org/10.5194/amt-3-579-2010, 2010.

Cappa, C. D. and Jimenez, J. L.: Quantitative estimates of the volatility of ambient organic aerosol, Atmos. Chem. Phys., 10, 5409–5424, https://doi.org/10.5194/acp-10-5409-2010, 2010.

Carslaw, K. S., Lee, L. A., Reddington, C. L., Pringle, K. J., Rap, A., Forster, P. M., Mann, G. W., Spracklen, D. V., Woodhouse, M. T., Regayre, L. A., and Pierce, J. R.: Large contribution of natural aerosols to uncertainty in indirect forcing, Nature, 503, 67–71, https://doi.org/10.1038/nature12674, 2013.

Cerully, K. M., Raatikainen, T., Lance, S., Tkacik, D., Tiitta, P., Petäjä, T., Ehn, M., Kulmala, M., Worsnop, D. R., Laaksonen, A., Smith, J. N., and Nenes, A.: Aerosol hygroscopicity and CCN activation kinetics in a boreal forest environment during the 2007 EUCAARI campaign, Atmospheric Chemistry and Physics, 11, 12369–12386, https://doi.org/10.5194/acp-11-12369-2011, 2011.

Connolly, P. J., Topping, D. O., Malavelle, F., and McFiggans, G.: A parameterisation for the activation of cloud drops including the effects of semi-volatile organics, Atmos. Chem. Phys., 14, 2289–2302, https://doi.org/10.5194/acp-14-2289-2014, 2014.

Crooks, M., Connolly, P., and McFiggans, G.: A parameterisation for the co-condensation of semi-volatile organics into multiple aerosol particle modes, Geosci. Model Dev., 11, 3261–3278, https://doi.org/10.5194/gmd-11-3261-2018, 2018.

Dada, L., Paasonen, P., Nieminen, T., Buenrostro Mazon, S., Kontkanen, J., Peräkylä, O., Lehtipalo, K., Hussein, T., Petäjä, T., Kerminen, V.-M., Bäck, J., and Kulmala, M.: Long-term analysis of clear-sky new particle formation events and nonevents in Hyytiälä, Atmos. Chem. Phys., 17, 6227–6241, https://doi.org/10.5194/acp-17-6227-2017, 2017.

Daumit, K. E., Kessler, S. H., and Kroll, J. H.: Average chemical properties and potential formation pathways of highly oxidized organic aerosol, Faraday Discuss., 165, 181–202, https://doi.org/10.1039/C3FD00045A, 2013.

Donahue, N. M., Robinson, A. L., Stanier, C. O., and Pandis, S. N.: Coupled Partitioning, Dilution, and Chemical Aging of Semivolatile Organics, Environ. Sci. Technol., 40, 2635–2643, https://doi.org/10.1021/es052297c, 2006.

Donahue, N. M., Epstein, S. A., Pandis, S. N., and Robinson, A. L.: A two-dimensional volatility basis set: 1. organic-aerosol mixing thermodynamics, Atmos. Chem. Phys., 11, 3303–3318, https://doi.org/10.5194/acp-11-3303-2011, 2011.

Epstein, S. A., Riipinen, I., and Donahue, N. M.: A Semiempirical Correlation between Enthalpy of Vaporization and Saturation Concentration for Organic Aerosol, Environ. Sci. Technol., 44, 743–748, https://doi.org/10.1021/es902497z, 2010.

1267 Forster, P., Storelvmo, T., Armour, K., Collins, W., Dufresne, J.-L., Frame, D., Lunt, D. J., Mauritsen,
1268 T., Palmer, M. D., Watanabe, M., Wild, M., and Zhang, H.: The Earth's energy budget, climate
1269 feedbacks, and climate sensitivity, in: Climate Change 2021: The Physical Science Basis.
1270 Contribution of Working Group I to the Sixth Assessment Report of the Intergovernmental Panel on
1271 Climate Change, edited by: Masson-Delmotte, V., Zhai, P., Pirani, A., Connors, S. L., Péan, C.,
1272 Berger, S., Caud, N., Chen, Y., Goldfarb, L., Gomis, M. I., Huang, M., Leitzell, K., Lonnoy, E.,
1273 Matthews, J. B. R., Maycock, T. K., Waterfield, T., Yelekçi, Ö., Yu, R., and Zhou, B., Cambridge
1274 University Press, 2021.

1275 Fredenslund, A., Jones, R. L., and Prausnitz, J. M.: Group-contribution estimation of activity
1276 coefficients in nonideal liquid mixtures, AIChE Journal, 21, 1086–1099,
1277 https://doi.org/10.1002/aic.690210607, 1975.

1278 Galloway, J. N., Likens, G. E., Keene, W. C., and Miller, J. M.: The composition of precipitation in
1279 remote areas of the world, Journal of Geophysical Research: Oceans, 87, 8771–8786,
1280 https://doi.org/10.1029/JC087iC11p08771, 1982.

1281 Graham, E. L., Wu, C., Bell, D. M., Bertrand, A., Haslett, S. L., Baltensperger, U., El Haddad, I.,
1282 Krejci, R., Riipinen, I., and Mohr, C.: Volatility of aerosol particles from NO_3 oxidation of various
1283 biogenic organic precursors, EGUsphere, 1–22, https://doi.org/10.5194/egusphere-2022-1043, 2022.

1284 Guenther, A., Hewitt, C. N., Erickson, D., Fall, R., Geron, C., Graedel, T., Harley, P., Klinger, L.,
1285 Lerdau, M., Mckay, W. A., Pierce, T., Scholes, B., Steinbrecher, R., Tallamraju, R., Taylor, J., and
1286 Zimmerman, P.: A global model of natural volatile organic compound emissions, Journal of
1287 Geophysical Research: Atmospheres, 100, 8873–8892, https://doi.org/10.1029/94JD02950, 1995.

1288 Guenther, A. B., Zimmerman, P. R., Harley, P. C., Monson, R. K., and Fall, R.: Isoprene and
1289 monoterpene emission rate variability: Model evaluations and sensitivity analyses, Journal of
1290 Geophysical Research: Atmospheres, 98, 12609–12617, https://doi.org/10.1029/93JD00527, 1993.

1291 Gunthe, S. S., Liu, P., Panda, U., Raj, S. S., Sharma, A., Darbyshire, E., Reyes-Villegas, E., Allan, J.,
1292 Chen, Y., Wang, X., Song, S., Pöhlker, M. L., Shi, L., Wang, Y., Kommula, S. M., Liu, T., Ravikrishna,
1293 R., McFiggans, G., Mickley, L. J., Martin, S. T., Pöschl, U., Andreae, M. O., and Coe, H.: Enhanced
1294 aerosol particle growth sustained by high continental chlorine emission in India, Nat. Geosci., 14, 77–
1295 84, https://doi.org/10.1038/s41561-020-00677-x, 2021.

1296 Hakola, H., Hellén, H., Hemmilä, M., Rinne, J., and Kulmala, M.: In situ measurements of volatile
1297 organic compounds in a boreal forest, Atmos. Chem. Phys., 12, 11665–11678,
1298 https://doi.org/10.5194/acp-12-11665-2012, 2012.

1299 Hallquist, M., Wenger, J. C., Baltensperger, U., Rudich, Y., Simpson, D., Claeys, M., Dommen, J.,
1300 Donahue, N. M., George, C., Goldstein, A. H., Hamilton, J. F., Herrmann, H., Hoffmann, T., Iinuma,
1301 Y., Jang, M., Jenkin, M. E., Jimenez, J. L., Kiendler-Scharr, A., Maenhaut, W., McFiggans, G., Mentel,
1302 T. F., Monod, A., Prévôt, A. S. H., Seinfeld, J. H., Surratt, J. D., Szmigielski, R., and Wildt, J.: The
1303 formation, properties and impact of secondary organic aerosol: current and emerging issues,
1304 Atmospheric Chemistry and Physics, 9, 5155–5236, https://doi.org/10.5194/acp-9-5155-2009, 2009.

1305 Hänel, G.: The role of aerosol properties during the condensational stage of cloud: A reinvestigation
1306 of numerics and microphysics, Beitr. Phys. Atmos., 60, 321–339, 1987.

1307 Hari, P. and Kulmala, M.: Station for Measuring Ecosystem–Atmosphere Relations (SMEAR II),
1308 Boreal Environ. Res., 10, 8, 2005.

1309 Hegg, D. A.: Impact of gas-phase HNO3 and NH3 on microphysical processes in atmospheric clouds,
1310 Geophysical Research Letters, 27, 2201–2204, https://doi.org/10.1029/1999GL011252, 2000.

1311 Heikkinen, L., Äijälä, M., Riva, M., Luoma, K., Daellenbach, K., Aalto, J., Aalto, P., Aliaga, D., Aurela,
1312 M., Keskinen, H., Makkonen, U., Rantala, P., Kulmala, M., Petäjä, T., Worsnop, D., and Ehn, M.:
1313 Long-term sub-micrometer aerosol chemical composition in the boreal forest: inter- and intra-annual
1314 variability, Atmos. Chem. Phys., 20, 3151–3180, https://doi.org/10.5194/acp-20-3151-2020, 2020.

1315 Heikkinen, L., Äijälä, M., Daellenbach, K. R., Chen, G., Garmash, O., Aliaga, D., Graeffe, F., Räty, M.,
1316 Luoma, K., Aalto, P., Kulmala, M., Petäjä, T., Worsnop, D., and Ehn, M.: Eight years of sub-
1317 micrometre organic aerosol composition data from the boreal forest characterized using a machine-
1318 learning approach, Atmos. Chem. Phys., 21, 10081–10109, https://doi.org/10.5194/acp-21-10081-
1319 2021, 2021.

1320 Hong, J., Häkkinen, S. a. K., Paramonov, M., Äijälä, M., Hakala, J., Nieminen, T., Mikkilä, J., Prisle, N.
1321 L., Kulmala, M., Riipinen, I., Bilde, M., Kerminen, V.-M., and Petäjä, T.: Hygroscopicity, CCN and
1322 volatility properties of submicron atmospheric aerosol in a boreal forest environment during the
1323 summer of 2010, Atmospheric Chemistry and Physics, 14, 4733–4748, https://doi.org/10.5194/acp-
1324 14-4733-2014, 2014.

1325 Hoppel, W. A. and Frick, G. M.: Submicron aerosol size distributions measured over the tropical and
1326 South Pacific, Atmospheric Environment. Part A. General Topics, 24, 645–659,
1327 https://doi.org/10.1016/0960-1686(90)90020-N, 1990.

1328 Hu, D., Topping, D., and McFiggans, G.: Measured particle water uptake enhanced by co-condensing
1329 vapours, Atmospheric Chemistry and Physics, 18, 14925–14937, https://doi.org/10.5194/acp-18-
1330 14925-2018, 2018.

1331 Huang, W., Li, H., Sarnela, N., Heikkinen, L., Tham, Y. J., Mikkilä, J., Thomas, S. J., Donahue, N. M.,
1332 Kulmala, M., and Bianchi, F.: Measurement report: Molecular composition and volatility of gaseous
1333 organic compounds in a boreal forest – from volatile organic compounds to highly oxygenated organic
1334 molecules, Atmos. Chem. Phys., 21, 8961–8977, https://doi.org/10.5194/acp-21-8961-2021, 2021.

1335 Huffman, J. A., Docherty, K. S., Aiken, A. C., Cubison, M. J., Ulbrich, I. M., DeCarlo, P. F., Sueper, D.,
1336 Jayne, J. T., Worsnop, D. R., Ziemann, P. J., and Jimenez, J. L.: Chemically-resolved aerosol
1337 volatility measurements from two megacity field studies, Atmos. Chem. Phys., 9, 7161–7182,
1338 https://doi.org/10.5194/acp-9-7161-2009, 2009a.

1339 Huffman, J. A., Docherty, K. S., Mohr, C., Cubison, M. J., Ulbrich, I. M., Ziemann, P. J., Onasch, T. B.,
1340 and Jimenez, J. L.: Chemically-Resolved Volatility Measurements of Organic Aerosol from Different
1341 Sources, Environ. Sci. Technol., 43, 5351–5357, https://doi.org/10.1021/es803539d, 2009b.

1342 Hunter, J. F., Day, D. A., Palm, B. B., Yatavelli, R. L. N., Chan, A. W. H., Kaser, L., Cappellin, L.,
1343 Hayes, P. L., Cross, E. S., Carrasquillo, A. J., Campuzano-Jost, P., Stark, H., Zhao, Y., Hohaus, T.,
1344 Smith, J. N., Hansel, A., Karl, T., Goldstein, A. H., Guenther, A., Worsnop, D. R., Thornton, J. A.,
1345 Heald, C. L., Jimenez, J. L., and Kroll, J. H.: Comprehensive characterization of atmospheric organic
1346 carbon at a forested site, Nature Geosci, 10, 748–753, https://doi.org/10.1038/ngeo3018, 2017.

1347 Hussein, T., Maso, M. D., Petäjä, T., Koponen, I. K., Paatero, P., Aalto, P. P., Hämeri, K., and
1348 Kulmala, M.: Evaluation of an automatic algorithm for fitting the particle number size distributions,
1349 Boreal Environ. Res., 10, 19, 2005.

1350 Isaacman-VanWertz, G. and Aumont, B.: Impact of organic molecular structure on the estimation of
1351 atmospherically relevant physicochemical parameters, Atmos. Chem. Phys., 21, 6541–6563,
1352 https://doi.org/10.5194/acp-21-6541-2021, 2021.

1353 Kakavas, S., Pandis, S. N., and Nenes, A.: ISORROPIA-Lite: A Comprehensive Atmospheric Aerosol
1354 Thermodynamics Module for Earth System Models, Tellus B: Chemical and Physical Meteorology, 74,
1355 1–23, https://doi.org/10.16993/tellusb.33, 2022.

1356 Kerminen, V.-M., Chen, X., Vakkari, V., Petäjä, T., Kulmala, M., and Bianchi, F.: Atmospheric new
1357 particle formation and growth: review of field observations, Environ. Res. Lett., 13, 103003,
1358 https://doi.org/10.1088/1748-9326/aadf3c, 2018.

1359 Kim, P., Partridge, D. G., and Haywood, J.: Constraining the model representation of the aerosol life
1360 cycle in relation to sources and sinks, EGU General Assembly 2020, Online, 4–8 May 2020,
1361 EGU2020-21948, https://doi.org/10.5194/egusphere-egu2020-21948, 2020.

Köhler, H.: The nucleus in and the growth of hygroscopic droplets, Trans. Faraday Soc., 32, 1152–1161, https://doi.org/10.1039/TF9363201152, 1936.

Kontkanen, J., Paasonen, P., Aalto, J., Bäck, J., Rantala, P., Petäjä, T., and Kulmala, M.: Simple proxies for estimating the concentrations of monoterpenes and their oxidation products at a boreal forest site, Atmospheric Chemistry and Physics, 16, 13291–13307, https://doi.org/10.5194/acp-16-13291-2016, 2016.

Korhonen, P., Kulmala, M., and Vesala, T.: Model simulation of the amount of soluble mass during cloud droplet formation, Atmospheric Environment, 30, 1773–1785, https://doi.org/10.1016/1352-2310(95)00380-0, 1996.

Kulmala, M., Laaksonen, A., Korhonen, P., Vesala, T., Ahonen, T., and Barrett, J. C.: The effect of atmospheric nitric acid vapor on cloud condensation nucleus activation, Journal of Geophysical Research: Atmospheres, 98, 22949–22958, https://doi.org/10.1029/93JD02070, 1993.

Kulmala, M., Rannik, Ü., Pirjola, L., Maso, M. D., Karimäki, J., Asmi, A., Jäppinen, A., Karhu, V., Korhonen, H., Malvikko, S.-P., Puustinen, A., Raittila, J., Romakkaniemi, S., Suni, T., Yli-Koivisto, S., Paatero, J., Hari, P., and Vesala, T.: Characterization of atmospheric trace gas and aerosol concentrations at forest sites in southern and northern Finland using back trajectories, Boreal Environ. Res., 5, 22, 2000.

Kulmala, M., Suni, T., Lehtinen, K. E. J., Dal Maso, M., Boy, M., Reissell, A., Rannik, Ü., Aalto, P., Keronen, P., Hakola, H., Bäck, J., Hoffmann, T., Vesala, T., and Hari, P.: A new feedback mechanism linking forests, aerosols, and climate, Atmospheric Chemistry and Physics, 4, 557–562, https://doi.org/10.5194/acp-4-557-2004, 2004.

Kulmala, M., Nieminen, T., Nikandrova, A., Lehtipalo, K., Manninen, H. E., Kajos, M. K., Kolari, P., Lauri, A., Petäjä, T., Krejci, R., Hansson, H.-C., Swietlicki, E., Lindroth, A., Christensen, T. R., Arneth, A., Hari, P., Bäck, J., Vesala, T., and Kerminen, V.-M.: CO2-induced terrestrial climate feedback mechanism: From carbon sink to aerosol source and back, Boreal Environ. Res., 19, 10, 2014.

Kyrö, E.-M., Väänänen, R., Kerminen, V.-M., Virkkula, A., Petäjä, T., Asmi, A., Dal Maso, M., Nieminen, T., Juhola, S., Shcherbinin, A., Riipinen, I., Lehtipalo, K., Keronen, P., Aalto, P. P., Hari, P., and Kulmala, M.: Trends in new particle formation in eastern Lapland, Finland: effect of decreasing sulfur emissions from Kola Peninsula, Atmos. Chem. Phys., 14, 4383–4396, https://doi.org/10.5194/acp-14-4383-2014, 2014.

Lee, B. H., Lopez-Hilfiker, F. D., D'Ambro, E. L., Zhou, P., Boy, M., Petäjä, T., Hao, L., Virtanen, A., and Thornton, J. A.: Semi-volatile and highly oxygenated gaseous and particulate organic compounds observed above a boreal forest canopy, Atmos. Chem. Phys., 18, 11547–11562, https://doi.org/10.5194/acp-18-11547-2018, 2018.

Lee, B. H., D'Ambro, E. L., Lopez-Hilfiker, F. D., Schobesberger, S., Mohr, C., Zawadowicz, M. A., Liu, J., Shilling, J. E., Hu, W., Palm, B. B., Jimenez, J. L., Hao, L., Virtanen, A., Zhang, H., Goldstein, A. H., Pye, H. O. T., and Thornton, J. A.: Resolving Ambient Organic Aerosol Formation and Aging Pathways with Simultaneous Molecular Composition and Volatility Observations, ACS Earth Space Chem., 4, 391–402, https://doi.org/10.1021/acsearthspacechem.9b00302, 2020.

Lee, I.-Y. and Pruppacher, H. R.: A comparative study on the growth of cloud drops by condensation using an air parcel model with and without entrainment, PAGEOPH, 115, 523–545, https://doi.org/10.1007/BF00876119, 1977.

Li, Y., Pöschl, U., and Shiraiwa, M.: Molecular corridors and parameterizations of volatility in the chemical evolution of organic aerosols, Atmos. Chem. Phys., 16, 3327–3344, https://doi.org/10.5194/acp-16-3327-2016, 2016.

Lohmann, U. and Feichter, J.: Global indirect aerosol effects: a review, Atmos. Chem. Phys., 23, 2005.

1409 Lopez-Hilfiker, F. D., Mohr, C., Ehn, M., Rubach, F., Kleist, E., Wildt, J., Mentel, T. F., Lutz, A.,
1410 Hallquist, M., Worsnop, D., and Thornton, J. A.: A novel method for online analysis of gas and particle
1411 composition: description and evaluation of a Filter Inlet for Gases and AEROsols (FIGAERO), Atmos.
1412 Meas. Tech., 7, 983–1001, https://doi.org/10.5194/amt-7-983-2014, 2014.

1413 Lopez-Hilfiker, F. D., Mohr, C., Ehn, M., Rubach, F., Kleist, E., Wildt, J., Mentel, T. F., Carrasquillo, A.
1414 J., Daumit, K. E., Hunter, J. F., Kroll, J. H., Worsnop, D. R., and Thornton, J. A.: Phase partitioning
1415 and volatility of secondary organic aerosol components formed from α-pinene ozonolysis and OH
1416 oxidation: the importance of accretion products and other low volatility compounds, Atmospheric
1417 Chemistry and Physics, 15, 7765–7776, https://doi.org/10.5194/acp-15-7765-2015, 2015.

1418 Lowe, S. J.: Modelling the effects of organic aerosol phase partitioning processes on cloud formation,
1419 PhD thesis, Stockholm University, Faculty of Science, Department of Environmental Science,
1420 Stockholm, Sweden, 2020.

1421 Lowe, S. J., Partridge, D. G., Davies, J. F., Wilson, K. R., Topping, D., and Riipinen, I.: Key drivers of
1422 cloud response to surface-active organics, Nat Commun, 10, 5214, https://doi.org/10.1038/s41467-
1423 019-12982-0, 2019.

1424 Luoma, K.: AEROSOL OPTICAL PROPERTIES, BLACK CARBON AND THEIR SPATIO-TEMPORAL
1425 VARIATION, PhD thesis, University of Helsinki, 2021.

1426 Lutz, A., Mohr, C., Le Breton, M., Lopez-Hilfiker, F. D., Priestley, M., Thornton, J. A., and Hallquist,
1427 M.: Gas to Particle Partitioning of Organic Acids in the Boreal Atmosphere, ACS Earth Space Chem.,
1428 3, 1279–1287, https://doi.org/10.1021/acsearthspacechem.9b00041, 2019.

1429 Mann, G. W., Carslaw, K. S., Spracklen, D. V., Ridley, D. A., Manktelow, P. T., Chipperfield, M. P.,
1430 Pickering, S. J., and Johnson, C. E.: Description and evaluation of GLOMAP-mode: a modal global
1431 aerosol microphysics model for the UKCA composition-climate model, Geoscientific Model
1432 Development, 3, 519–551, https://doi.org/10.5194/gmd-3-519-2010, 2010.

1433 Mikhailov, E. F., Mironova, S., Mironov, G., Vlasenko, S., Panov, A., Chi, X., Walter, D., Carbone, S.,
1434 Artaxo, P., Heimann, M., Lavric, J., Pöschl, U., and Andreae, M. O.: Long-term measurements (2010–
1435 2014) of carbonaceous aerosol and carbon monoxide at the Zotino Tall Tower Observatory (ZOTTO)
1436 in central Siberia, Atmos. Chem. Phys., 17, 14365–14392, https://doi.org/10.5194/acp-17-14365-
1437 2017, 2017.

1438 Millet, D. B., Baasandorj, M., Farmer, D. K., Thornton, J. A., Baumann, K., Brophy, P., Chaliyakunnel,
1439 S., de Gouw, J. A., Graus, M., Hu, L., Koss, A., Lee, B. H., Lopez-Hilfiker, F. D., Neuman, J. A.,
1440 Paulot, F., Peischl, J., Pollack, I. B., Ryerson, T. B., Warneke, C., Williams, B. J., and Xu, J.: A large
1441 and ubiquitous source of atmospheric formic acid, Atmos. Chem. Phys., 15, 6283–6304,
1442 https://doi.org/10.5194/acp-15-6283-2015, 2015.

1443 Mohr, C., Lopez-Hilfiker, F. D., Yli-Juuti, T., Heitto, A., Lutz, A., Hallquist, M., D'Ambro, E. L.,
1444 Rissanen, M. P., Hao, L., Schobesberger, S., Kulmala, M., Mauldin III, R. L., Makkonen, U., Sipilä, M.,
1445 Petäjä, T., and Thornton, J. A.: Ambient observations of dimers from terpene oxidation in the gas
1446 phase: Implications for new particle formation and growth, Geophysical Research Letters, 44, 2958–
1447 2966, https://doi.org/10.1002/2017GL072718, 2017.

1448 Mohr, C., Thornton, J. A., Heitto, A., Lopez-Hilfiker, F. D., Lutz, A., Riipinen, I., Hong, J., Donahue, N.
1449 M., Hallquist, M., Petäjä, T., Kulmala, M., and Yli-Juuti, T.: Molecular identification of organic vapors
1450 driving atmospheric nanoparticle growth, Nat Commun, 10, 4442, https://doi.org/10.1038/s41467-019-
1451 12473-2, 2019.

1452 Mulcahy, J. P., Jones, C., Sellar, A., Johnson, B., Boutle, I. A., Jones, A., Andrews, T., Rumbold, S.
1453 T., Mollard, J., Bellouin, N., Johnson, C. E., Williams, K. D., Grosvenor, D. P., and McCoy, D. T.:
1454 Improved Aerosol Processes and Effective Radiative Forcing in HadGEM3 and UKESM1, Journal of
1455 Advances in Modeling Earth Systems, 10, 2786–2805, https://doi.org/10.1029/2018MS001464, 2018.

Mulcahy, J. P., Johnson, C., Jones, C. G., Povey, A. C., Scott, C. E., Sellar, A., Turnock, S. T., Woodhouse, M. T., Abraham, N. L., Andrews, M. B., Bellouin, N., Browse, J., Carslaw, K. S., Dalvi, M., Folberth, G. A., Glover, M., Grosvenor, D. P., Hardacre, C., Hill, R., Johnson, B., Jones, A., Kipling, Z., Mann, G., Mollard, J., O'Connor, F. M., Palmiéri, J., Reddington, C., Rumbold, S. T., Richardson, M., Schutgens, N. A. J., Stier, P., Stringer, M., Tang, Y., Walton, J., Woodward, S., and Yool, A.: Description and evaluation of aerosol in UKESM1 and HadGEM3-GC3.1 CMIP6 historical simulations, Geosci. Model Dev., 13, 6383–6423, https://doi.org/10.5194/gmd-13-6383-2020, 2020.

Murphy, B. N., Julin, J., Riipinen, I., and Ekman, A. M. L.: Organic aerosol processing in tropical deep convective clouds: Development of a new model (CRM-ORG) and implications for sources of particle number, Journal of Geophysical Research: Atmospheres, 120, 10,441-10,464, https://doi.org/10.1002/2015JD023551, 2015.

Ng, N. L., Herndon, S. C., Trimborn, A., Canagaratna, M. R., Croteau, P. L., Onasch, T. B., Sueper, D., Worsnop, D. R., Zhang, Q., Sun, Y. L., and Jayne, J. T.: An Aerosol Chemical Speciation Monitor (ACSM) for Routine Monitoring of the Composition and Mass Concentrations of Ambient Aerosol, Aerosol Science and Technology, 45, 780–794, https://doi.org/10.1080/02786826.2011.560211, 2011.

Nieminen, T., Asmi, A., Maso, M. D., Aalto, P. P., Keronen, P., Petäjä, T., Kulmala, M., and Kerminen, V.-M.: Trends in atmospheric new-particle formation: 16 years of observations in a boreal-forest environment, Boreal Environ. Res., 19, 191–214, 2014.

NIST Chemistry WebBook: https://webbook.nist.gov/cgi/cbook.cgi?ID=C64186&Mask=4, last access: 8 November 2022.

Ovadnevaite, J., Zuend, A., Laaksonen, A., Sanchez, K. J., Roberts, G., Ceburnis, D., Decesari, S., Rinaldi, M., Hodas, N., Facchini, M. C., Seinfeld, J. H., and O' Dowd, C.: Surface tension prevails over solute effect in organic-influenced cloud droplet activation, Nature, 546, 637–641, https://doi.org/10.1038/nature22806, 2017.

Paasonen, P., Asmi, A., Petäjä, T., Kajos, M. K., Äijälä, M., Junninen, H., Holst, T., Abbatt, J. P. D., Arneth, A., Birmili, W., van der Gon, H. D., Hamed, A., Hoffer, A., Laakso, L., Laaksonen, A., Richard Leaitch, W., Plass-Dülmer, C., Pryor, S. C., Räisänen, P., Swietlicki, E., Wiedensohler, A., Worsnop, D. R., Kerminen, V.-M., and Kulmala, M.: Warming-induced increase in aerosol number concentration likely to moderate climate change, Nature Geosci, 6, 438–442, https://doi.org/10.1038/ngeo1800, 2013.

Pankow, J. F., Seinfeld, J. H., Asher, W. E., and Erdakos, G. B.: Modeling the Formation of Secondary Organic Aerosol. 1. Application of Theoretical Principles to Measurements Obtained in the α-Pinene/, β-Pinene/, Sabinene/, Δ3-Carene/, and Cyclohexene/Ozone Systems, Environ. Sci. Technol., 35, 1164–1172, https://doi.org/10.1021/es001321d, 2001.

Paramonov, M., Aalto, P. P., Asmi, A., Prisle, N., Kerminen, V.-M., Kulmala, M., and Petäjä, T.: The analysis of size-segregated cloud condensation nuclei counter (CCNC) data and its implications for cloud droplet activation, Atmos. Chem. Phys., 13, 10285–10301, https://doi.org/10.5194/acp-13-10285-2013, 2013.

Paramonov, M., Kerminen, V.-M., Gysel, M., Aalto, P. P., Andreae, M. O., Asmi, E., Baltensperger, U., Bougiatioti, A., Brus, D., Frank, G. P., Good, N., Gunthe, S. S., Hao, L., Irwin, M., Jaatinen, A., Jurányi, Z., King, S. M., Kortelainen, A., Kristensson, A., Lihavainen, H., Kulmala, M., Lohmann, U., Martin, S. T., McFiggans, G., Mihalopoulos, N., Nenes, A., O'Dowd, C. D., Ovadnevaite, J., Petäjä, T., Pöschl, U., Roberts, G. C., Rose, D., Svenningsson, B., Swietlicki, E., Weingartner, E., Whitehead, J., Wiedensohler, A., Wittbom, C., and Sierau, B.: A synthesis of cloud condensation nuclei counter (CCNC) measurements within the EUCAARI network, Atmospheric Chemistry and Physics, 15, 12211–12229, https://doi.org/10.5194/acp-15-12211-2015, 2015.

Partridge, D., Morales, R., and Stier, P.: Comparing droplet activation parameterisations against adiabatic parcel models using a novel inverse modelling framework, EGU General Assembly Conference Abstracts, ADS Bibcode: 2015EGUGA..1714019P, 14019, 2015.

Partridge, D. G., Vrugt, J. A., Tunved, P., Ekman, A. M. L., Gorea, D., and Sorooshian, A.: Inverse modeling of cloud-aerosol interactions – Part 1: Detailed response surface analysis, Atmos. Chem. Phys., 11, 7269–7287, https://doi.org/10.5194/acp-11-7269-2011, 2011.

Partridge, D. G., Vrugt, J. A., Tunved, P., Ekman, A. M. L., Struthers, H., and Sorooshian, A.: Inverse modelling of cloud-aerosol interactions – Part 2: Sensitivity tests on liquid phase clouds using a Markov chain Monte Carlo based simulation approach, Atmos. Chem. Phys., 12, 2823–2847, https://doi.org/10.5194/acp-12-2823-2012, 2012.

Peng, Y., Lohmann, U., and Leaitch, R.: Importance of vertical velocity variations in the cloud droplet nucleation process of marine stratus clouds, Journal of Geophysical Research: Atmospheres, 110, https://doi.org/10.1029/2004JD004922, 2005.

Petäjä, T., O'Connor, E. J., Moisseev, D., Sinclair, V. A., Manninen, A. J., Väänänen, R., Lerber, A. von, Thornton, J. A., Nicoll, K., Petersen, W., Chandrasekar, V., Smith, J. N., Winkler, P. M., Krüger, O., Hakola, H., Timonen, H., Brus, D., Laurila, T., Asmi, E., Riekkola, M.-L., Mona, L., Massoli, P., Engelmann, R., Komppula, M., Wang, J., Kuang, C., Bäck, J., Virtanen, A., Levula, J., Ritsche, M., and Hickmon, N.: BAECC: A Field Campaign to Elucidate the Impact of Biogenic Aerosols on Clouds and Climate, Bulletin of the American Meteorological Society, 97, 1909–1928, https://doi.org/10.1175/BAMS-D-14-00199.1, 2016.

Petäjä, T., Tabakova, K., Manninen, A., Ezhova, E., O'Connor, E., Moisseev, D., Sinclair, V. A., Backman, J., Levula, J., Luoma, K., Virkkula, A., Paramonov, M., Räty, M., Äijälä, M., Heikkinen, L., Ehn, M., Sipilä, M., Yli-Juuti, T., Virtanen, A., Ritsche, M., Hickmon, N., Pulik, G., Rosenfeld, D., Worsnop, D. R., Bäck, J., Kulmala, M., and Kerminen, V.-M.: Influence of biogenic emissions from boreal forests on aerosol–cloud interactions, Nat. Geosci., 15, 42–47, https://doi.org/10.1038/s41561-021-00876-0, 2022.

Petters, M. D. and Kreidenweis, S. M.: A single parameter representation of hygroscopic growth and cloud condensation nucleus activity – Part 2: Including solubility, Atmos. Chem. Phys., 7, 2008.

Pruppacher, H. R. and Klett, J. D.: Microphysics of Clouds and Precipitation, Springer Netherlands, Dordrecht, https://doi.org/10.1007/978-0-306-48100-0, 1997.

Ridley, J. K., Blockley, E. W., Keen, A. B., Rae, J. G. L., West, A. E., and Schroeder, D.: The sea ice model component of HadGEM3-GC3.1, Geoscientific Model Development, 11, 713–723, https://doi.org/10.5194/gmd-11-713-2018, 2018.

Roelofs, G. J. H.: Drop size dependent sulfate distribution in a growing cloud, J Atmos Chem, 14, 109–118, https://doi.org/10.1007/BF00115227, 1992a.

Roelofs, G. J. H.: On the drop and aerosol size dependence of aqueous sulfate formation in a continental cumulus cloud, Atmospheric Environment. Part A. General Topics, 26, 2309–2321, https://doi.org/10.1016/0960-1686(92)90362-O, 1992b.

Roelofs, G.-J. and Jongen, S.: A model study of the influence of aerosol size and chemical properties on precipitation formation in warm clouds, J. Geophys. Res., 109, https://doi.org/10.1029/2004JD004779, 2004.

Romakkaniemi, S., Kokkola, H., and Laaksonen, A.: Parameterization of the nitric acid effect on CCN activation, Atmospheric Chemistry and Physics, 5, 879–885, https://doi.org/10.5194/acp-5-879-2005, 2005.

Ruehl, C. R., Chuang, P. Y., Nenes, A., Cappa, C. D., Kolesar, K. R., and Goldstein, A. H.: Strong evidence of surface tension reduction in microscopic aqueous droplets, Geophysical Research Letters, 39, https://doi.org/10.1029/2012GL053706, 2012.

Ruehl, C. R., Davies, J. F., and Wilson, K. R.: An interfacial mechanism for cloud droplet formation on organic aerosols, Science, 351, 1447–1450, https://doi.org/10.1126/science.aad4889, 2016.

1552 Schobesberger, S., Lopez-Hilfiker, F. D., Taipale, D., Millet, D. B., D'Ambro, E. L., Rantala, P.,
1553 Mammarella, I., Zhou, P., Wolfe, G. M., Lee, B. H., Boy, M., and Thornton, J. A.: High upward fluxes
1554 of formic acid from a boreal forest canopy, Geophysical Research Letters, 43, 9342–9351,
1555 https://doi.org/10.1002/2016GL069599, 2016.

1556 Scott, C. E., Arnold, S. R., Monks, S. A., Asmi, A., Paasonen, P., and Spracklen, D. V.: Substantial
1557 large-scale feedbacks between natural aerosols and climate, Nature Geosci, 11, 44–48,
1558 https://doi.org/10.1038/s41561-017-0020-5, 2018.

1559 Sellar, A. A., Jones, C. G., Mulcahy, J. P., Tang, Y., Yool, A., Wiltshire, A., O'Connor, F. M., Stringer,
1560 M., Hill, R., Palmieri, J., Woodward, S., de Mora, L., Kuhlbrodt, T., Rumbold, S. T., Kelley, D. I., Ellis,
1561 R., Johnson, C. E., Walton, J., Abraham, N. L., Andrews, M. B., Andrews, T., Archibald, A. T.,
1562 Berthou, S., Burke, E., Blockley, E., Carslaw, K., Dalvi, M., Edwards, J., Folberth, G. A., Gedney, N.,
1563 Griffiths, P. T., Harper, A. B., Hendry, M. A., Hewitt, A. J., Johnson, B., Jones, A., Jones, C. D.,
1564 Keeble, J., Liddicoat, S., Morgenstern, O., Parker, R. J., Predoi, V., Robertson, E., Siahaan, A.,
1565 Smith, R. S., Swaminathan, R., Woodhouse, M. T., Zeng, G., and Zerroukat, M.: UKESM1:
1566 Description and Evaluation of the U.K. Earth System Model, Journal of Advances in Modeling Earth
1567 Systems, 11, 4513–4558, https://doi.org/10.1029/2019MS001739, 2019.

1568 Sellar, A. A., Walton, J., Jones, C. G., Wood, R., Abraham, N. L., Andrejczuk, M., Andrews, M. B.,
1569 Andrews, T., Archibald, A. T., de Mora, L., Dyson, H., Elkington, M., Ellis, R., Florek, P., Good, P.,
1570 Gohar, L., Haddad, S., Hardiman, S. C., Hogan, E., Iwi, A., Jones, C. D., Johnson, B., Kelley, D. I.,
1571 Kettleborough, J., Knight, J. R., Köhler, M. O., Kuhlbrodt, T., Liddicoat, S., Linova-Pavlova, I.,
1572 Mizielinski, M. S., Morgenstern, O., Mulcahy, J., Neininger, E., O'Connor, F. M., Petrie, R., Ridley, J.,
1573 Rioual, J.-C., Roberts, M., Robertson, E., Rumbold, S., Seddon, J., Shepherd, H., Shim, S.,
1574 Stephens, A., Teixiera, J. C., Tang, Y., Williams, J., Wiltshire, A., and Griffiths, P. T.: Implementation
1575 of U.K. Earth System Models for CMIP6, Journal of Advances in Modeling Earth Systems, 12,
1576 e2019MS001946, https://doi.org/10.1029/2019MS001946, 2020.

1577 Shrivastava, M., Cappa, C. D., Fan, J., Goldstein, A. H., Guenther, A. B., Jimenez, J. L., Kuang, C.,
1578 Laskin, A., Martin, S. T., Ng, N. L., Petaja, T., Pierce, J. R., Rasch, P. J., Roldin, P., Seinfeld, J. H.,
1579 Shilling, J., Smith, J. N., Thornton, J. A., Volkamer, R., Wang, J., Worsnop, D. R., Zaveri, R. A.,
1580 Zelenyuk, A., and Zhang, Q.: Recent advances in understanding secondary organic aerosol:
1581 Implications for global climate forcing, Reviews of Geophysics, 55, 509–559,
1582 https://doi.org/10.1002/2016RG000540, 2017.

1583 Sihto, S.-L., Mikkilä, J., Vanhanen, J., Ehn, M., Liao, L., Lehtipalo, K., Aalto, P. P., Duplissy, J.,
1584 Petäjä, T., Kerminen, V.-M., Boy, M., and Kulmala, M.: Seasonal variation of CCN concentrations and
1585 aerosol activation properties in boreal forest, Atmospheric Chemistry and Physics, 11, 13269–13285,
1586 https://doi.org/10.5194/acp-11-13269-2011, 2011.

1587 Simpson, E., Connolly, P., and McFiggans, G.: An investigation into the performance of four cloud
1588 droplet activation parameterisations, Geoscientific Model Development, 7, 1535–1542,
1589 https://doi.org/10.5194/gmd-7-1535-2014, 2014.

1590 Sporre, M. K., Blichner, S. M., Karset, I. H. H., Makkonen, R., and Berntsen, T. K.: BVOC–aerosol–
1591 climate feedbacks investigated using NorESM, Atmospheric Chemistry and Physics, 19, 4763–4782,
1592 https://doi.org/10.5194/acp-19-4763-2019, 2019.

1593 Sporre, M. K., Blichner, S. M., Schrödner, R., Karset, I. H. H., Berntsen, T. K., van Noije, T., Bergman,
1594 T., O'Donnell, D., and Makkonen, R.: Large difference in aerosol radiative effects from BVOC-SOA
1595 treatment in three Earth system models, Atmospheric Chemistry and Physics, 20, 8953–8973,
1596 https://doi.org/10.5194/acp-20-8953-2020, 2020.

1597 Spracklen, D. V., Bonn, B., and Carslaw, K. S.: Boreal forests, aerosols and the impacts on clouds
1598 and climate, Philosophical Transactions of the Royal Society A: Mathematical, Physical and
1599 Engineering Sciences, 366, 4613–4626, https://doi.org/10.1098/rsta.2008.0201, 2008.

1600 Storkey, D., Blaker, A. T., Mathiot, P., Megann, A., Aksenov, Y., Blockley, E. W., Calvert, D., Graham,
1601 T., Hewitt, H. T., Hyder, P., Kuhlbrodt, T., Rae, J. G. L., and Sinha, B.: UK Global Ocean GO6 and

GO7: a traceable hierarchy of model resolutions, Geoscientific Model Development, 11, 3187–3213, https://doi.org/10.5194/gmd-11-3187-2018, 2018.

Thornhill, G., Collins, W., Olivié, D., Skeie, R. B., Archibald, A., Bauer, S., Checa-Garcia, R., Fiedler, S., Folberth, G., Gjermundsen, A., Horowitz, L., Lamarque, J.-F., Michou, M., Mulcahy, J., Nabat, P., Naik, V., O'Connor, F. M., Paulot, F., Schulz, M., Scott, C. E., Séférian, R., Smith, C., Takemura, T., Tilmes, S., Tsigaridis, K., and Weber, J.: Climate-driven chemistry and aerosol feedbacks in CMIP6 Earth system models, Atmospheric Chemistry and Physics, 21, 1105–1126, https://doi.org/10.5194/acp-21-1105-2021, 2021.

Thornton, J. A., Mohr, C., Schobesberger, S., D'Ambro, E. L., Lee, B. H., and Lopez-Hilfiker, F. D.: Evaluating Organic Aerosol Sources and Evolution with a Combined Molecular Composition and Volatility Framework Using the Filter Inlet for Gases and Aerosols (FIGAERO), Acc. Chem. Res., 53, 1415–1426, https://doi.org/10.1021/acs.accounts.0c00259, 2020.

Topping, D., Connolly, P., and McFiggans, G.: Cloud droplet number enhanced by co-condensation of organic vapours, Nature Geosci, 6, 443–446, https://doi.org/10.1038/ngeo1809, 2013.

Topping, D. O. and McFiggans, G.: Tight coupling of particle size, number and composition in atmospheric cloud droplet activation, Atmospheric Chemistry and Physics, 12, 3253–3260, https://doi.org/10.5194/acp-12-3253-2012, 2012.

Tunved, P., Hansson, H.-C., Kerminen, V.-M., Ström, J., Maso, M. D., Lihavainen, H., Viisanen, Y., Aalto, P. P., Komppula, M., and Kulmala, M.: High Natural Aerosol Loading over Boreal Forests, Science, 312, 261–263, https://doi.org/10.1126/science.1123052, 2006.

Turnock, S. T., Allen, R. J., Andrews, M., Bauer, S. E., Deushi, M., Emmons, L., Good, P., Horowitz, L., John, J. G., Michou, M., Nabat, P., Naik, V., Neubauer, D., O'Connor, F. M., Olivié, D., Oshima, N., Schulz, M., Sellar, A., Shim, S., Takemura, T., Tilmes, S., Tsigaridis, K., Wu, T., and Zhang, J.: Historical and future changes in air pollutants from CMIP6 models, Atmospheric Chemistry and Physics, 20, 14547–14579, https://doi.org/10.5194/acp-20-14547-2020, 2020.

Twomey, S.: Pollution and the planetary albedo, Atmospheric Environment (1967), 8, 1251–1256, https://doi.org/10.1016/0004-6981(74)90004-3, 1974.

Twomey, S.: The Influence of Pollution on the Shortwave Albedo of Clouds, Journal of the Atmospheric Sciences, 34, 1149–1152, https://doi.org/10.1175/1520-0469(1977)034<1149:TIOPOT>2.0.CO;2, 1977.

Vehkamäki, H., Kulmala, M., Napari, I., Lehtinen, K. E. J., Timmreck, C., Noppel, M., and Laaksonen, A.: An improved parameterization for sulfuric acid–water nucleation rates for tropospheric and stratospheric conditions, Journal of Geophysical Research: Atmospheres, 107, AAC 3-1-AAC 3-10, https://doi.org/10.1029/2002JD002184, 2002.

Walters, D., Boutle, I., Brooks, M., Melvin, T., Stratton, R., Vosper, S., Wells, H., Williams, K., Wood, N., Allen, T., Bushell, A., Copsey, D., Earnshaw, P., Edwards, J., Gross, M., Hardiman, S., Harris, C., Heming, J., Klingaman, N., Levine, R., Manners, J., Martin, G., Milton, S., Mittermaier, M., Morcrette, C., Riddick, T., Roberts, M., Sanchez, C., Selwood, P., Stirling, A., Smith, C., Suri, D., Tennant, W., Vidale, P. L., Wilkinson, J., Willett, M., Woolnough, S., and Xavier, P.: The Met Office Unified Model Global Atmosphere 6.0/6.1 and JULES Global Land 6.0/6.1 configurations, Geoscientific Model Development, 10, 1487–1520, https://doi.org/10.5194/gmd-10-1487-2017, 2017.

Wang, Y., Chen, Y., Wu, Z., Shang, D., Bian, Y., Du, Z., Schmitt, S. H., Su, R., Gkatzelis, G. I., Schlag, P., Hohaus, T., Voliotis, A., Lu, K., Zeng, L., Zhao, C., Alfarra, M. R., McFiggans, G., Wiedensohler, A., Kiendler-Scharr, A., Zhang, Y., and Hu, M.: Mutual promotion between aerosol particle liquid water and particulate nitrate enhancement leads to severe nitrate-dominated particulate matter pollution and low visibility, Atmospheric Chemistry and Physics, 20, 2161–2175, https://doi.org/10.5194/acp-20-2161-2020, 2020.

1649 West, R. E. L., Stier, P., Jones, A., Johnson, C. E., Mann, G. W., Bellouin, N., Partridge, D. G., and
1650 Kipling, Z.: The importance of vertical velocity variability for estimates of the indirect aerosol effects,
1651 Atmos. Chem. Phys., 14, 6369–6393, https://doi.org/10.5194/acp-14-6369-2014, 2014.

1652 Williams, J., Crowley, J., Fischer, H., Harder, H., Martinez, M., Petäjä, T., Rinne, J., Bäck, J., Boy, M.,
1653 Dal Maso, M., Hakala, J., Kajos, M., Keronen, P., Rantala, P., Aalto, J., Aaltonen, H., Paatero, J.,
1654 Vesala, T., Hakola, H., Levula, J., Pohja, T., Herrmann, F., Auld, J., Mesarchaki, E., Song, W.,
1655 Yassaa, N., Nölscher, A., Johnson, A. M., Custer, T., Sinha, V., Thieser, J., Pouvesle, N., Taraborrelli,
1656 D., Tang, M. J., Bozem, H., Hosaynali-Beygi, Z., Axinte, R., Oswald, R., Novelli, A., Kubistin, D.,
1657 Hens, K., Javed, U., Trawny, K., Breitenberger, C., Hidalgo, P. J., Ebben, C. J., Geiger, F. M.,
1658 Corrigan, A. L., Russell, L. M., Ouwersloot, H. G., Vilà-Guerau de Arellano, J., Ganzeveld, L., Vogel,
1659 A., Beck, M., Bayerle, A., Kampf, C. J., Bertelmann, M., Köllner, F., Hoffmann, T., Valverde, J.,
1660 González, D., Riekkola, M.-L., Kulmala, M., and Lelieveld, J.: The summertime Boreal forest field
1661 measurement intensive (HUMPPA-COPEC-2010): an overview of meteorological and chemical
1662 influences, Atmos. Chem. Phys., 11, 10599–10618, https://doi.org/10.5194/acp-11-10599-2011, 2011.

1663 Yan, C., Nie, W., Äijälä, M., Rissanen, M. P., Canagaratna, M. R., Massoli, P., Junninen, H., Jokinen,
1664 T., Sarnela, N., Häme, S. A. K., Schobesberger, S., Canonaco, F., Yao, L., Prévôt, A. S. H., Petäjä,
1665 T., Kulmala, M., Sipilä, M., Worsnop, D. R., and Ehn, M.: Source characterization of highly oxidized
1666 multifunctional compounds in a boreal forest environment using positive matrix factorization, Atmos.
1667 Chem. Phys., 16, 12715–12731, https://doi.org/10.5194/acp-16-12715-2016, 2016.

1668 Yatavelli, R. L. N., Mohr, C., Stark, H., Day, D. A., Thompson, S. L., Lopez-Hilfiker, F. D.,
1669 Campuzano-Jost, P., Palm, B. B., Vogel, A. L., Hoffmann, T., Heikkinen, L., Äijälä, M., Ng, N. L.,
1670 Kimmel, J. R., Canagaratna, M. R., Ehn, M., Junninen, H., Cubison, M. J., Petäjä, T., Kulmala, M.,
1671 Jayne, J. T., Worsnop, D. R., and Jimenez, J. L.: Estimating the contribution of organic acids to
1672 northern hemispheric continental organic aerosol, Geophysical Research Letters, 42, 6084–6090,
1673 https://doi.org/10.1002/2015GL064650, 2015.

1674 Yli-Juuti, T., Mielonen, T., Heikkinen, L., Arola, A., Ehn, M., Isokääntä, S., Keskinen, H.-M., Kulmala,
1675 M., Laakso, A., Lipponen, A., Luoma, K., Mikkonen, S., Nieminen, T., Paasonen, P., Petäjä, T.,
1676 Romakkaniemi, S., Tonttila, J., Kokkola, H., and Virtanen, A.: Significance of the organic aerosol
1677 driven climate feedback in the boreal area, Nat Commun, 12, 5637, https://doi.org/10.1038/s41467-
1678 021-25850-7, 2021.

1679 Ylivinkka, I., Kaupinmäki, S., Virman, M., Peltola, M., Taipale, D., Petäjä, T., Kerminen, V.-M.,
1680 Kulmala, M., and Ezhova, E.: Clouds over Hyytiälä, Finland: an algorithm to classify clouds based on
1681 solar radiation and cloud base height measurements, Atmospheric Measurement Techniques, 13,
1682 5595–5619, https://doi.org/10.5194/amt-13-5595-2020, 2020.

1683 Zhang, Y., Peräkylä, O., Yan, C., Heikkinen, L., Äijälä, M., Daellenbach, K. R., Zha, Q., Riva, M.,
1684 Garmash, O., Junninen, H., Paatero, P., Worsnop, D., and Ehn, M.: Insights into atmospheric
1685 oxidation processes by performing factor analyses on subranges of mass spectra, Atmos. Chem.
1686 Phys., 20, 5945–5961, https://doi.org/10.5194/acp-20-5945-2020, 2020.

1687